Journal of Medicinal Chemistry

pubs.acs.org/jmc

Article

Structure-Based Discovery of Imidazo[4,5-*c*]pyridine SARM1 Modulators Showing Paradoxical Activation

Steven K. Albanese, Brittany E. Hopkins, Andrea M. Olland, Alexis Fairman, Nadim Shaikh, Shulu Feng, Mahesh Thakkar, Andreas Verras, Alexey Dementiev, Ward G. Walkup, 4th, Christian Atsriku, Harathi D. Srinivas, Wayne Allen, Khuram Ashraf, Pieter H. Bos, Peng Hsiao, Kyle Kroeck, Zhijian Liu, Anu Nagarajan, Christopher T. Szlenk, Mats Svensson, Zachary Lee Johnson, Kanishk Kapilashrami, Stephen Rubino, Andrew Kaplan, and Adam M. Levinson*

Cite This: *J. Med. Chem.* 2026, 69, 9521−9536

Read Online

ACCESS | Metrics & More | Article Recommendations | Supporting Information

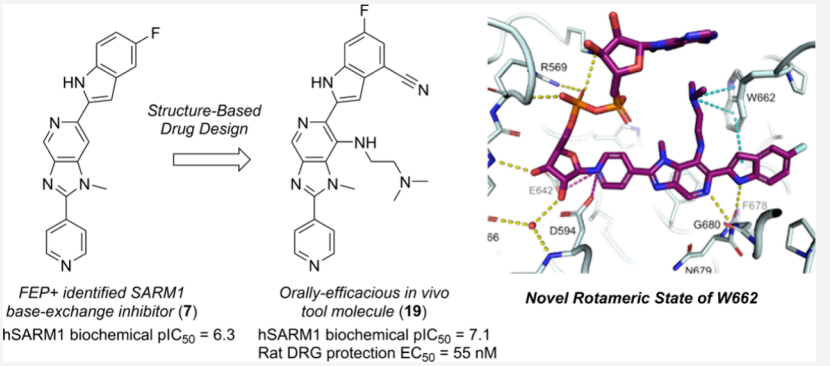

ABSTRACT: Sterile Alpha and TIR Motif Containing 1 (SARM1) is an NAD^+ hydrolase enzyme implicated in neurological diseases with prominent axonopathies. A reported method for SARM1 inhibition involves the design of small molecules bearing reactive heterocyclic warheads, which intercept the hydrolysis of NAD^+ in the active site of SARM1 and subsequently inhibit enzymatic function of the TIR domain. Herein, we describe the discovery of a series of bicyclic SARM1 inhibitors, initially identified via a unique workflow for free-energy perturbation (FEP+) simulations. Subsequent hit expansion efforts identified potent and cell-active inhibitors with slow off-rates, which impart a unique conformational state of W662 in the SARM1 catalytic site, as assessed via X-ray crystallography. Finally, we discuss an identified liability associated with substrate-based SARM1 inhibitors such as **19**, whereby insufficient target engagement results in an increase in biomarkers of neurodegeneration at low doses *in vivo* and exacerbates neuronal degeneration and cell death *in vitro*.

INTRODUCTION

Wallerian-like degeneration and axonopathies are common pathophysiological features that are found in many neurological diseases. This degeneration is a tightly controlled cellular process that is mediated by the NADase SARM1.[1−3] SARM1 is an octamer, with each subunit containing a mitochondrial targeting sequence (MTS) at the N-terminus followed by an armadillo repeat (ARM) domain, two tandem sterile α motif (SAM) domains, and a Toll/interleukin (TIR)-1 receptor (TIR) domain at the C-terminus. SARM1 exerts its role as an axon executioner by sensing the intracellular levels of nicotinamide adenine dinucleotide (NAD^+) and nicotinamide mononucleotide (NMN). When NAD^+ levels are high under normal conditions, NAD^+ binds to the ARM domains and maintains SARM1 in an inactive state.[1,3,4] When levels of NAD^+ fall and NMN levels increase following cellular perturbations, NMN binds to the ARM domains, which release the TIR domains, allowing them to form a double-stranded assembly with enzymatically active NADase sites at the interfaces of neighboring TIR subunits. This in turn results in degeneration of the axon and ultimately cell death.[1,3,5]

Because of the central role of SARM1 in axon degeneration, it is an attractive therapeutic target. One class of small molecule inhibitors, base exchange inhibitors (BEIs) such as **1**−**5**, binds to the active site at the interface of TIR domain subunits and forms an adduct with NAD^+ (Figure 1).[6−10]

Received: February 2, 2026
Revised: March 20, 2026
Accepted: March 26, 2026
Published: April 8, 2026

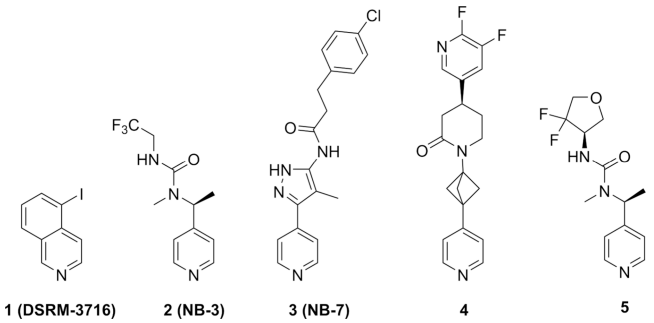

Figure 1. Representative reported inhibitors of SARM1-bearing reactive warheads.

These BEIs have shown robust protection against axonal degeneration in various *in vitro* assays. *In vivo* studies have shown that SARM1 inhibitors provide axonal protection, reduce serum neurofilament light chain (NfL) release, and alleviate neuropathic pain in models of chemotherapy induced peripheral neuropathy (CIPN) and peripheral sciatic nerve axotomy.[6−8,10,11] These demonstrated that the benefits of pharmacological SARM1 inhibition are consistent with SARM1 knockout animals, knock down, and antisense oligonucleotides.[12−14]

Herein, we report a computational modeling workflow to discover novel BEIs for the treatment of neurodegenerative disorders and our ultimate discovery of a series of potent, novel SARM1 inhibitors that induce a previously undescribed rotameric state of W662. Finally, we describe an observation whereby our BEIs demonstrate paradoxical neurodegenerative effects at subinhibitory concentrations *in vitro* and *in vivo*, an effect that others have recently described to have clinical implications in the development of BEIs of SARM1.[8,10,15−19]

RESULTS

Novel Workflow Enabled Ideation and Modeling of Base Exchange Inhibitor Designs

Common to previously reported SARM1 BEI scaffolds is an unsubstituted pyridine warhead, which reacts with NAD^+ to generate the adenosine diphosphate ribose (ADPR)-bound active site inhibitor. The reactive nature of SARM1 BEIs presents a unique challenge for computational modeling. New molecular designs drawn by chemists do not reflect the structure of the nucleotide-bound adduct that inhibits the enzyme. While nonconjugated BEIs would be the appropriate species for predicting physicochemical and druglike properties in ligand design, they are not best suited for active site docking, let alone for use in relative free-energy binding calculations,

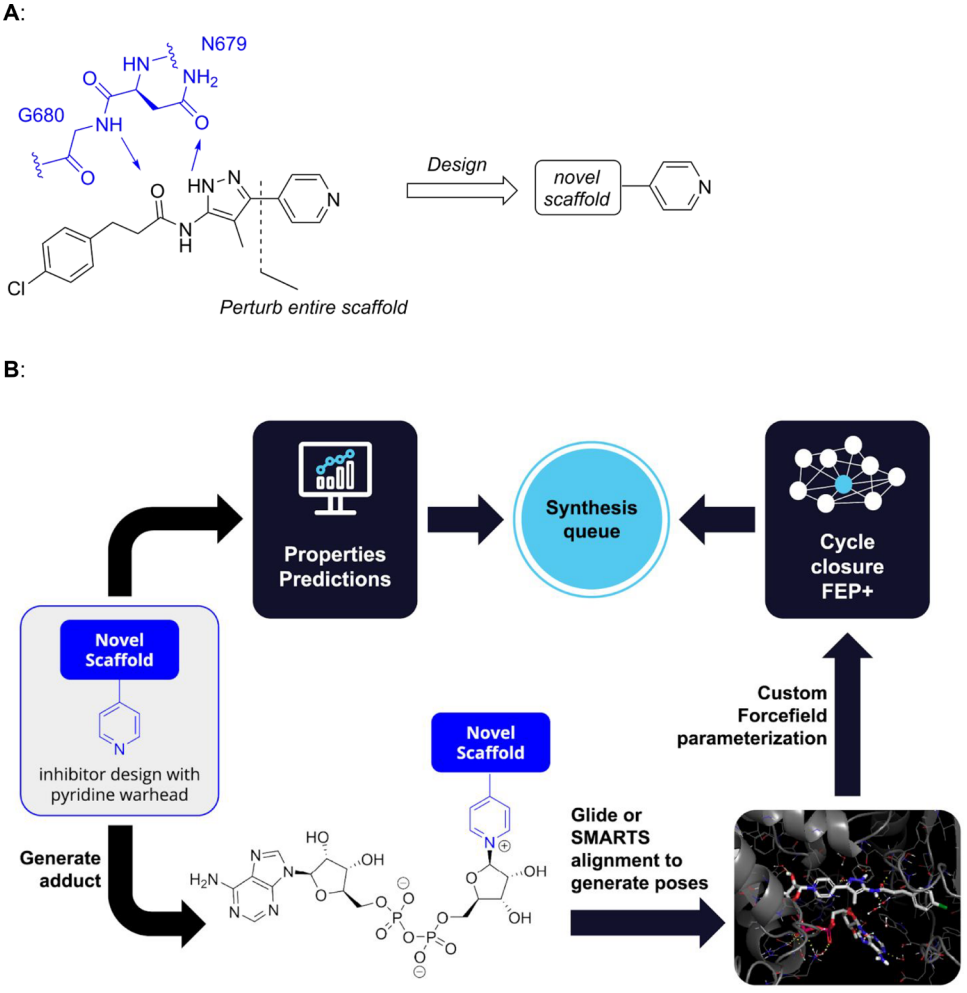

Figure 2. Design and FEP+ modeling concepts to identify new scaffolds that inhibit SARM1. (A) Design strategy to modify the scaffold of NB-7 while maintaining the pyridine reactive warhead. (B) Modeling work flow using a covalent docking approach.

https://doi.org/10.1021/acs.jmedchem.6c00352
J. Med. Chem. 2026, 69, 9521−9536

Table 1. Initial Discovery of New SARM1 Inhibitor Scaffolds Using FEP+[a]

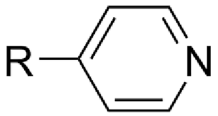

Cpd #	R	NAD-Glo pIC_{50}	FEP+ pIC_{50}	LogD (LLE)	Kinetic Solubility (pH 7.4) [μM]
6	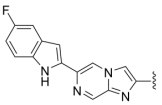	6.7 (n=3)	8.6	4.1 (2.6)	<0.005
7	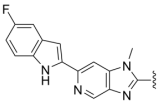	6.3 (n=4)	6.8	3.3 (3)	<0.8
8	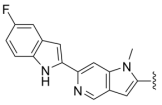	5.6 (n=1)	5.4	4.3* (1.3)	ND
9	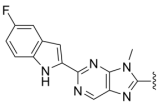	5.2 (n=1)	6.3	3.4* (1.8)	ND
10	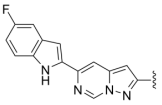	7.1 (n=1)	7.0	4.6* (2.6)	ND
11	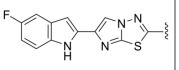	6.5 (n=1)	ND	4.3* (2.2)	ND
12	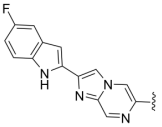	6.8 (n=2)	6.8	3.8 (3)	<0.24
13	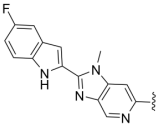	6.4 (n=1)	6.0	3.7* (2.7)	ND

[a]* denotes predicted LogD value.

such as FEP+.[20,21] This assumption was based on previous reports, which demonstrated that compounds **2** and **3** do not have appreciable binding affinity for SARM1-TIR in the absence of an NAD^+ cofactor, which suggests that any method by which binding is modeled would require the full ADPR-conjugated adduct.[7] To this end, we developed a unique flow scheme whereby scientists could design a novel BEI with the design prompt in Figure 2A, utilizing **3** (NB-7, PDB entry 8D0D) as a starting point and allowing redesign of the entire molecule beyond the pyridine warhead. In order to predict the potency of compounds, each design was conjugated to ADPR using the reaction SMARTS based tool Pathfinder to create the conjugated adduct.[22] The full adduct was then aligned into the binding site using maximum common substructure (MCS) or SMARTS-based alignments tools in Maestro.[23] Custom torsion parameters were generated on the entire adduct using Force Field Builder, prior to running in FEP+ (Figure 2B).[24]

Discovery of a Heterobicyclic SARM1 BEI Scaffold

Among the many design directions our team followed, one idea was to convert the pyrazole amide of NB-7 (**3**) into a bicyclic scaffold. NB-7 maintains an intramolecular hydrogen bond between the pyrazole NH and the adjacent amide carbonyl, with these moieties interacting with N679 and G680, respectively (Figure 2A). Replacement of this motif with a bicycle could theoretically maintain binding to SARM1, providing a new template for inhibitor discovery. As a caveat, this strategy would remove a hydrogen bond between the pyrazole NH and N679 but was envisioned to maintain binding to G680 if a heteroatom was placed in a similar space as the carbonyl oxygen of NB-7. We also recognized nearby

https://doi.org/10.1021/acs.jmedchem.6c00352
J. Med. Chem. 2026, 69, 9521−9536

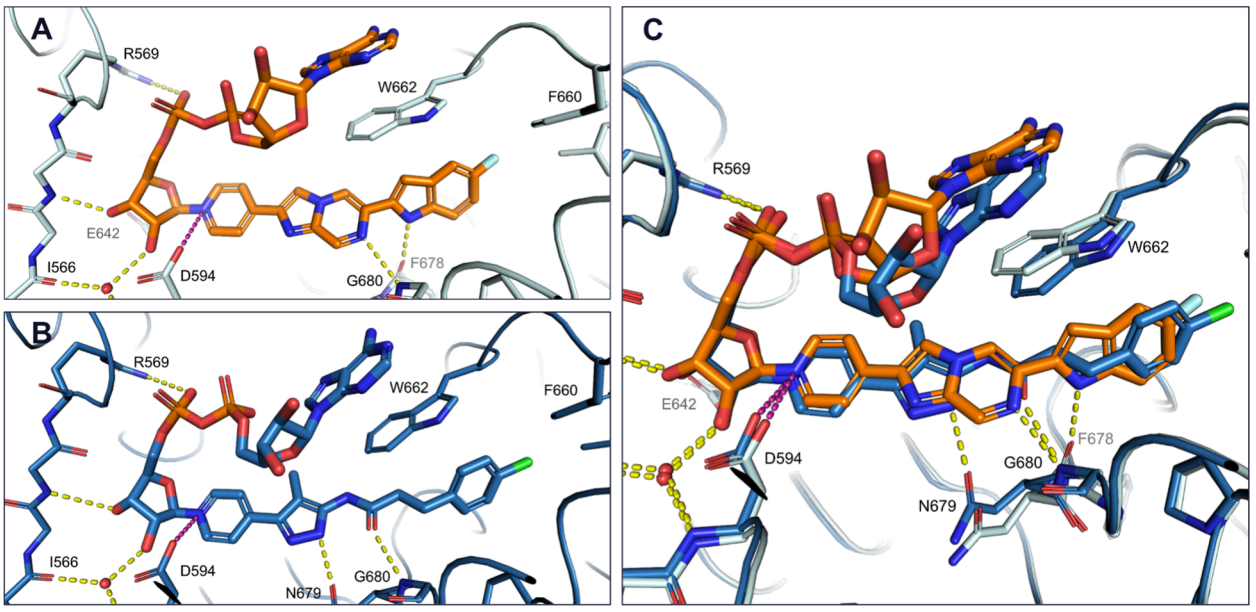

Figure 3. Structure of **6** bound to SARM1 at the interface between TIR-domains, determined by X-ray crystallography. (A) Cocrystal structure of **6** (1.79 Å; PDB: 10RA). (B) The published structure of **3** (PDB: 8D0D), shown for comparison. (C) Overlay of **6** with **3**. Yellow dashes denote hydrogen bonds, and magenta dashes denote salt bridges.

F678 as an unexplored hydrogen bonding partner, which could further anchor inhibitor binding to SARM1.

To this end, several novel scaffolds attached to the 4-position of a pyridine warhead were designed and profiled using the modeling workflow described in Figure 2B. One of the initial compounds made was **6** (Table 1), based on both a favorable FEP+ score (FEP+ pIC_{50} = 8.6) and the observed stable interactions between G680 and the imidazo[1,2-*a*]pyrazine core along with F678 and the terminal indole ring during the molecular dynamics simulation. Experimentally, we were pleased to see nanomolar enzymatic inhibition (pIC_{50} = 6.7), as assessed by a biochemical assay measuring NAD^+ levels using NAD-Glo. Although this was a case of FEP+ over-prediction, we were encouraged by this initial hit-finding result, given the significant molecular perturbation involved in this prediction. An X-ray crystal structure of **6** bound to the TIR domain of SARM1 (Figure 3A) was solved, revealing a binding mode similar to that initially hypothesized. The ADPR base-exchange adduct of **6** is observed, with key contacts between the ligand and the protein including a hydrogen bond between the imidazo[1,2-*a*]pyrazine core and G680, as well as a hydrogen bond between the indole NH and F678. An overlay of this structure with the published structure of **3** (NB-7, Figure 3B,C) reveals an overall similar space-filling within the binding site. The binding of **6** is largely similar to that of NB-7, differing by the expected loss of an H bond to N679, one H bond gained with F678, and an outward shift of W662 and the adenosine moiety to accommodate the fluoroindole of **6** while still maintaining the $\pi-\pi$ sandwich configuration seen with NB-7. Consistent with this binding mode, direct analogs of **6** replacing the hydrogen bond donor in the indole ring with either *N*-methyl or sulfur were also tested, and both demonstrated an IC_{50} of greater than 30 μM in the enzymatic assay (data not shown).

With this initial result in hand, additional core changes were explored. Bicyclic heterocyclic analogs **7**−**10** were synthesized and assessed in the NAD-Glo assay, demonstrating overall favorable predictivity from FEP+. Of note, 1-methyl-1*H*-imidazo[4,5-*c*]pyridine **7** stood out to us for its favorable NAD-Glo activity (pIC_{50} = 6.3) but relatively lower lipophilicity compared to **6**, which we anticipated would allow us to explore other vectors on the scaffold with more freedom in co-optimization of potency and ADME properties. We found that either removal of one nitrogen in the imidazole ring (**8**) or addition of a nitrogen atom (**9**) into this scaffold resulted in an unfavorable loss in biochemical potency. Pyrazolo[1,5-*c*]pyrimidine **10** showed an impressive gain in biochemical potency to under 100 nM IC_{50}, but it was among the more lipophilic scaffolds we assessed, demonstrating little apparent benefit from a lipophilic ligand efficiency (LLE) standpoint.

Lastly, we also explored changing the topology of the bicyclic core while maintaining a hydrogen bond acceptor available to interact with G680. To this end, both [5,5] and [5,6] ring systems appeared to be tolerated. Imidazo[2,1-*b*][1,3,4]thiadiazole **11** retained nanomolar activity in the NAD-Glo assay, as did both **12** and **13**. Notably, **12** and **13** are direct analogs of **6** and **7**, respectively, with the central heterocycle flipped yet still plausibly interacting with G680. The diversity of tolerated heterocyclic ring systems enabled a multipronged hit expansion approach, focused on exploration of R group substitution and indole replacements in a variety of geometric configurations.

We next directed our attention to further expanding on compound **7**, which demonstrated relatively favorable log *D* (3.3) and LLE (3) compared to other examples in Table 1. Given the submicromolar activity of **7**, we were interested in testing its ability to provide protection against SARM1 mediated cell death. To do so, we utilized a HEK293 cell line expressing the SAM-TIR domains under control of an inducible promoter, such that when exposed to doxycycline, the constitutive activity of SAM-TIR would lead to cell death measured by Cell Titer-Glo (CTG). In this assay, **7** demonstrated weak protection against cell death (SAM-TIR HEK293 pEC_{50} = 5.2). A notable challenge with the initially identified active molecules in Table 1 is their extremely poor

https://doi.org/10.1021/acs.jmedchem.6c00352
J. Med. Chem. 2026, 69, 9521−9536

solubility, whereby compounds **6**, **7**, and **12** all demonstrate kinetic solubility <1 μM at pH 7.4. Our subsequent hit expansion strategy thus sought to identify a useful vector for incorporation of polar substituents, which would ideally further improve potency and solubility within this scaffold and thus allow for effective *in vitro* assay reliability.

Expansion of SAR around Compound 7

In examining the structure of **7** and through subsequent FEP+ calculations, we identified a new vector for growing substituents off the central azabenzimidazole ring system. Compound **14** was thus prioritized for its FEP+ score predicting nanomolar binding and through its incorporation of basic functionality, anticipated to increase solubility of the scaffold (Figure 4). Pleasingly, **14** demonstrated a pIC_{50} of 6.6

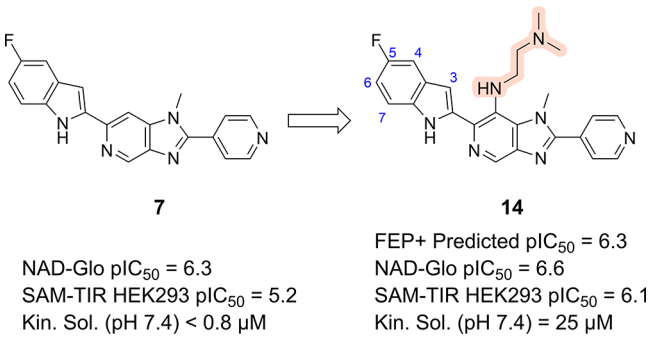

Figure 4. Discovery of a new substitution vector that improves cellular potency and kinetic solubility relative to initial hit **7**.

in the NAD-Glo assay and improved kinetic solubility from <0.8 to 25 μM. Even more notably, **14** fortuitously demonstrated submicromolar activity in the inducible SAM-TIR HEK293 assay (pEC_{50} = 6.1) and potent binding via surface plasmon resonance (SPR) (pK_D = 7.5).

While maintaining this ethylenediamine substitution, we explored the impact of the indole moiety (Table 2). Shifting the fluorine atom from C5 to C6 of the indole led to a further gain in potency in both biochemical and cellular assays, concurrent with an LLE increase to 4.6. Assessment via SPR revealed that the position of this fluorine atom had a significant impact on the off-rate of the BEIs, with **14** and **15** demonstrating residence half-lives of 710 and 8915 s, respectively (Supplemental Figure 1). This improvement in binding affinity was also reflected in a substantial improvement in protection observed in primary rat dorsal root ganglia (DRGs) treated with the chemotherapy drug vincristine (EC_{50} = 8.6 μM versus 613 nM, for compounds **14** and **15**, respectively). Replacement of the indole with benzimidazole **16** resulted in a loss of activity in NAD-Glo, inducible SAM-TIR HEK293, and SPR assays. Further exploration found that the ideal substitution pattern around the indole ring involved substitutions at C4 and C6, with difluoro analogue **17** further improving potency in biochemical and cellular assays relative to **15**. Replacement of the indole C4 substitution with a nitrile group identified **19**, with further improvement in the inducible SAM-TIR HEK293 assay (pEC_{50} = 7.8). We also found that 4-azaindole **18** is favorable for potency, but this substitution did impart efflux in a MDCK-MDR1 cell line (efflux ratio = 4.8).

A structure of **14** bound to the TIR domain active site of SARM1 was determined by X-ray crystallography (Figure 5A). Although **14** maintained similar interactions as **6** at the interface of two TIR domains, including H-bonds to G680 and F678 on one chain and salt bridges and H-bonds through the charged warhead and ribose moieties to the other chain, the ethylenediamine substituent displaced both W662 and the adenosine moiety of the BEI adduct, disrupting the $\pi-\pi$ stacking interactions between those and the fluoroindole of **6**. In the presence of the ethylenediamine substitution, W662 is rotated about 90° toward solvent to form a cation$-\pi$ interaction with the dimethylamine moiety and an edge-to-face π-stacking interaction with the fluoroindole (Figure 5C). We thus presumed that accessing this novel rotameric state of W662 might provide an opportunity to further expand accessible SAR both on the imidazo[4,5-*c*]pyridine core and on the terminal indole, whereby a new subpocket of SARM1 is opened relative to known inhibitors that is available for substituent exploration.

Given our initial observation that rotation of W662 opens a larger pocket accessible by the indole C4 position, we explored larger substitution to understand if filling out this pocket could lead to further potency gains. Accordingly, analogs **20**–**22** were synthesized to test this hypothesis, which were predicted to maintain or improve potency by FEP+. None of these analogs demonstrated any benefit across assays relative to **19**. However, the fact that these substitutions (including a large pyrimidine group in **22**) maintained submicromolar activity in biochemical and cellular assays was notable to us, given that one would not expect such large substitutions to be tolerated based on the published binding modes observed for **2** or **3**. An X-ray cocrystal structure of **22** further confirmed the assumed binding mode, whereby W662 is rotated to interact with the dimethylamino substituent, and the pyrimidine ring occupies the resulting induced pocket from that rotation (Figure 5B). Through the course of our exploration, it became apparent to us that the nature of substitutions on the azabenzimidazole and on the indole could be interdependent on one another, as each uniquely occupies space on opposite faces of the induced W662 indole rotamer.

The complexity of this flexible binding site was challenging for physics-based modeling. Using this FEP+ workflow allowed for the rapid identification of novel cores, with a prospective predictive performance of 0.6 pIC_{50} Mean Unsigned Error (MUE) across 22 compounds (data not shown). Despite the early success in hit finding, FEP+ performance was more modest when exploring further SAR expansion beyond **7**, with a prospective MUE of 0.78 pIC_{50} across 33 predictions for perturbations at the C7 position of the 1*H*-imidazo[4,5-*c*]pyridine core. FEP+ predictions were especially challenging when expanding at the C4 of the indole ring (examples **19**–**22**), with a prospective MUE of 1.1 pIC_{50} across 26 predictions. This may be attributed to several factors, including the induced rotation of W662 (Figure 5C), flexibility of the nucleotide portion of the ADPR adduct observed both in FEP + simulations and between X-ray structures, and the reactive nature of the BEI mechanism whereby the nonconjugated ligand binding and reaction rate are not accounted for in FEP+ simulations.

Compound **19** represented an interesting lead and demonstrated low nanomolar potency when tested for its ability to protect primary rat and mouse DRGs treated with vincristine (Supplemental Figure 2, EC_{50} 55 and 113 nM, respectively). Moreover, even with a basic amine and relatively high polar surface area (PSA = 95 Å^2), **19** demonstrated low efflux in an MDCK-MDR1 assay (Table 4) along with

https://doi.org/10.1021/acs.jmedchem.6c00352
J. Med. Chem. 2026, 69, 9521−9536

Table 2. Assessment of Indole Replacements on 14[a]

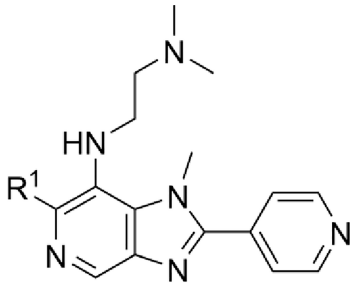

Cpd #	R1	FEP+ pIC_{50}	NAD-Glo pIC_{50}	LogD (LLE)	SAM-TIR HEK293 pEC_{50}	SPR pK_D / $t_{½}$ (sec)
14	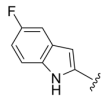	6.3	6.6 (n=3)	2.4 (4.2)	6.1 (n=3)	7.5 / 710
15	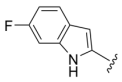	6.0	6.9 (n=1)	2.4 (4.6)	6.9 (n=4)	8.1 / 8,915
16	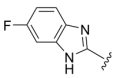	6.5	6.7 (n=1)	2.5 (4.2)	6.3 (n=2)	7.3 / 753
17	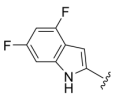	7.7	7.2 (n=2)	2.8 (4.4)	7.5 (n=2)	8.5 / 17,150
18	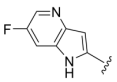	ND	6.8 (n=2)	1.8 (5)	7.0 (n=3)	8.4 / 25,100
19	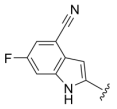	8.5	7.1 (n=3)	2.7 (4.3)	7.8 (n=5)	8.3 / 16,200
20	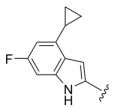	7.5	6.5 (n=1)	3.4* (3.1)	6.3 (n=2)	7.2 / 3,655
21	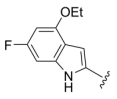	7.6	6.5 (n=1)	3.0* (3.5)	6.4 (n=2)	7.2 / 8,300
22	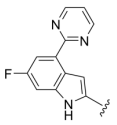	8.6	6.4 (n=1)	2.6 (3.9)	6.8 (n=2)	7.7 / 29,200

[a]* denotes predicted log *D* value.

moderate intrinsic clearance in both human and mouse liver microsomes, suggesting that it could serve as a useful tool molecule for *in vivo* neuroprotection assays. Similar to MDCK-MDR1, evaluation in a MDCK-BCRP cell line also showed an efflux ratio of 0.9. Consistent with liver microsomal stability, **19** demonstrated moderate clearance in mice (50 mL/min/kg), moderate volume of distribution (5 L/kg), and satisfactory oral bioavailability (34%) (Table 5). Moreover, upon oral dosing in mice at 30 mg/kg, we observed a $Kp_{uu,brain}$ of 0.26, highlighting that it is possible to achieve CNS exposure within

https://doi.org/10.1021/acs.jmedchem.6c00352
J. Med. Chem. 2026, 69, 9521−9536

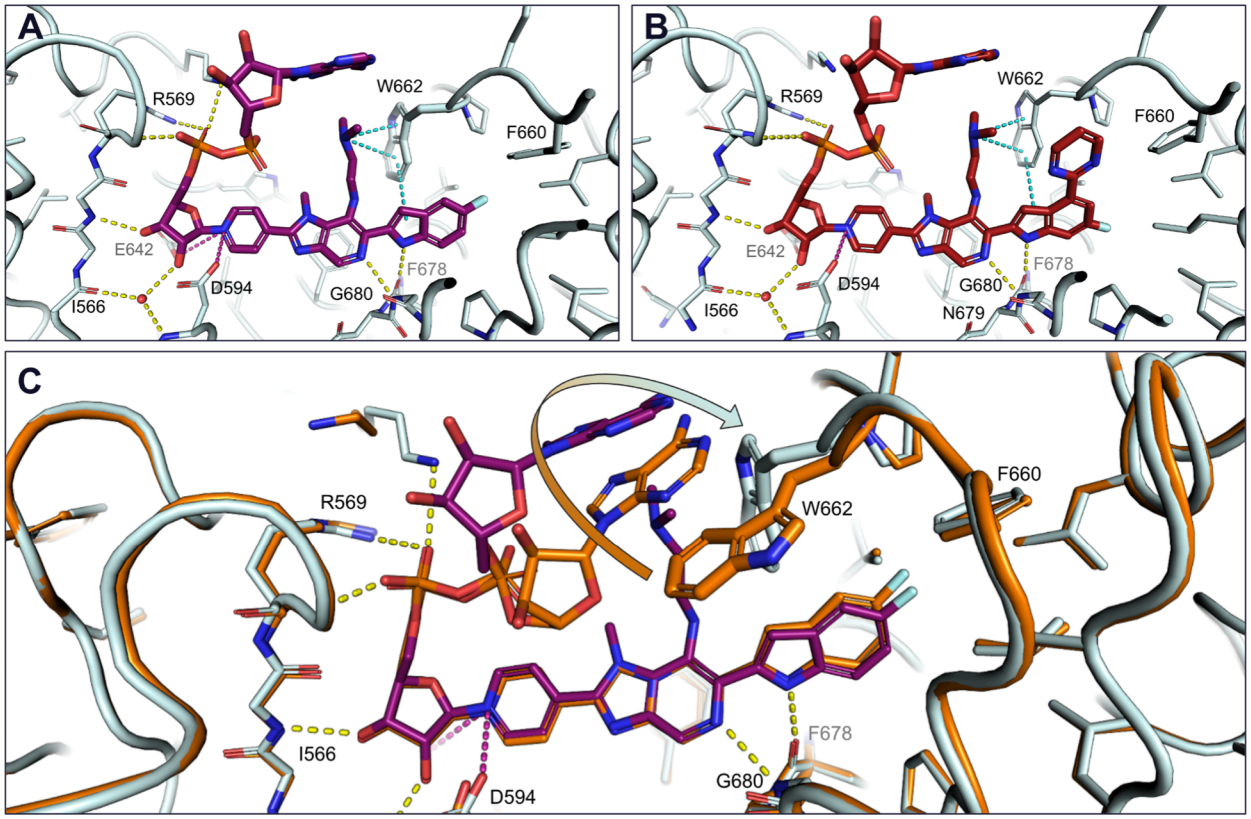

Figure 5. Cocrystal structures of representative inhibitors from Table 2 bound to SARM1 at the interface between the TIR-domains. (A) Structure of **14** (purple; 2.05 Å; PDB 10RB), which induces a novel rotamer of W662. (B) Structure of **22** (red; 1.90 Å; PDB 10RC) showing occupation of the pocket created by W662 rotation with a pyrimidine substituent. (C) Structure of **14** (purple) overlaid with **6** (orange). Yellow dashes denote hydrogen bonds; magenta dashes denote salt bridges, and cyan dashes denote pi interactions.

this series (Supplemental Figure 4). Unsurprisingly, we recognized early on that the 4-substituted pyridine warhead is a major liability for CYP inhibition, with **19** demonstrating an IC_{50} of less than 600 nM on CYP3A4 and 50 nM on CYP2D6. Also notable was the very potent inhibition of **19** against the human ether-a-go-go (hERG) channel (<1 μM), likely attributable to its highly aromatic and basic nature.

Several heterocyclic warhead replacements for the pyridine were explored in an effort to address the potent CYP inhibition observed but in most cases lost considerable potency compared to the unsubstituted pyridine. However, replacement of the pyridine with a pyridazine warhead proved to be successful. Compound **23**, a direct matched molecular pair to **19** bearing a pyridazine, maintained biochemical potency relative to the pyridine analog while further lowering Log *D* and improving biochemical LLE (Table 3). However, we did observe an approximately 3-fold loss in cellular potency relative to the pyridine analog. Remarkably, this single atom modification improved CYP3A4 inhibition from submicromolar IC_{50} to 15 μM (Table 4). CYP2D6 activity was also improved by over 10-fold, albeit still suboptimal (0.71 μM). Even with the addition of a heteroatom and lower Log *D*, **23** demonstrated high permeability (P_{app} A-B = 17 × 10^{-6}cm/s) with low efflux in an MDCK-MDR1 cell line, maintaining favorable CNS penetration potential. We recognized that the basic nature of R2 was likely a major liability in terms of the potent hERG activity observed, with **23** demonstrating similarly potent activity on hERG (0.47 μM) compared to **19**. In the course of our SAR, we extensively explored basic amines, including pK_a-attenuated analogs. However, nearly all examples maintained potent hERG inhibition.

Neutral R2 groups were also explored with the hopes of improving hERG and CYP2D6 inhibition (Table 3). FEP+ values are not provided for molecules in this table, as free energy calculations were not routinely run with warheads beyond the pyridine. *N*-Methyl-oxetane-3-amine **24** was made and found to retain biochemical activity, albeit with a loss of cellular activity. Interestingly, cellular activity was restored by pairing this neutral R2 group with an R1 group bearing a 5,7-difluoro substitution pattern (**25**). The preference for this R1 group is different compared to what was observed for amine-bearing analogs in Table 2, highlighting the likely interplay of R groups flanking either face of W662. In SPR, **25** also showed potent binding, with a K_D of 3 nM and long residence time ($t_{1/2}$ = 3.9 h). **25** demonstrated not only attenuated CYP3A4 inhibition (IC_{50} = 25.5 μM) but also mitigated liabilities on CYP2D6 (IC_{50} > 30 μM), for which basic amines are known preferred substrates (Table 4).[25] Although **25** did in fact show improvement in hERG inhibition relative to **19** and **23** (IC_{50} = 2.3 μM), additional modifications would be desired for further improvement. **25** also showed excellent metabolic stability in both human and mouse liver microsomes (CL_{int} < 3 mL/min/kg in human liver microsomes). Consistent with its favorable *in vitro* microsomal stability, **25** demonstrated low clearance in mice (15 mL/min/kg) with an improved half-life relative to **19** and high bioavailability (63%) (Table 5).

In exploring the space around the R2 vector, enlargement of the *N*-methyl-oxetane-3-amine R group to a tetrahydrofuran ring or extension of the methyl group to ethyl led to drops in

https://doi.org/10.1021/acs.jmedchem.6c00352
J. Med. Chem. 2026, 69, 9521−9536

Table 3. Representative Exploration of Neutral R Groups around the Azabenzimidazole Core Containing a Pyridazine Warhead[a]

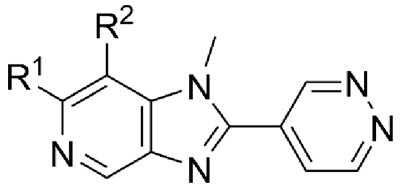

Cpd #	R1	R2	NAD-Glo pIC_{50}	LogD (LLE)	SAM-TIR HEK293 pEC_{50}
23	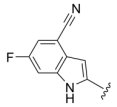		7.1 (n=1)	2.2 (4.9)	7.3 (n=3)
24	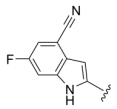		6.8 (n=1)	2.4* (4.4)	6.5 (n=2)
25	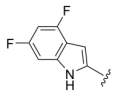		6.9 (n=1)	2.5 (4.4)	7.5 (n=2)
26	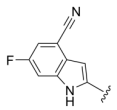		7.2 (n=1)	2.5* (4.8)	6.1 (n=2)
27	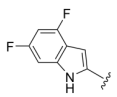		7.6 (n=2)	2.6* (4.9)	7.0 (n=3)
28	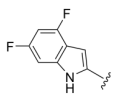		7.5 (n=2)	2.5 (5.1)	7.0 (n=3)

[a]* denotes predicted Log *D* value.

Table 4. *In Vitro* ADME Characterization

cpd #	MDCK-MDR1 Papp A→B [10^{-6}cm/s]; efflux ratio	h/m LM CL_{int} [mL/min/kg]	kinetic solubility (pH 7.4) [μM]	$F_{u,plasma}$ (mouse)	CYP IC_{50} [μM]	hERG IC_{50} [μM]
19	8.0; 1.2	30/126	6.0	0.12	3A4(M) = 0.6 2C9 = 13.6 2D6 = 0.05	<1
23	17.6; 0.9	14.9/117	3.2	0.21	3A4(M) = 15.6 2C9 > 30 2D6 = 0.71	0.47
25	8.8; 1.5	<3.1/42	11.1	0.12	3A4(M) = 25.5 2C9 > 30 2D6 > 30	2.32

Table 5. Mouse Pharmacokinetics for 19 and 25

compound	IV CL (CL_u)[a]	Vd_{ss}[b]	IV $t_{1/2}$[c]	%F
19	50 (417)	5.0	1.1	34
25	15 (125)	2.7	3.9	63

[a]Pharmacokinetics were assessed in fasted male C57BL/6 mice (n = 3) at doses of 2 mg/kg (IV) and 5 mg/kg (PO): mL/min/kg. [b]L/kg. [c]hours.

potency (data not shown), indicating the preference for relatively small R2 groups. Oxygen and des-methyl N linkers were also explored (examples **26**–**28**), with **27** and **28** demonstrating a slight improvement in biochemical activity relative to **25** but an approximately 0.5–0.6 log unit drop in potency in the inducible SAM-TIR HEK293 assay. Overall, **25** demonstrates promising *in vitro* and *in vivo* profiles with

https://doi.org/10.1021/acs.jmedchem.6c00352
J. Med. Chem. 2026, 69, 9521−9536

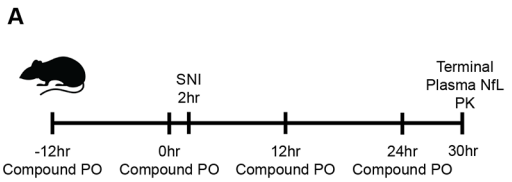

C

Compound, Dose	Plasma Concentration (ng/ml, 30hr)	TE Ratio
19, 25 mg/kg	285 ± 52	0.6
19, 50 mg/kg	903 ± 203	2.0
19, 100 mg/kg	3028 ± 1444	6.8
2, 100 mg/kg	26825 ± 3997	331.0

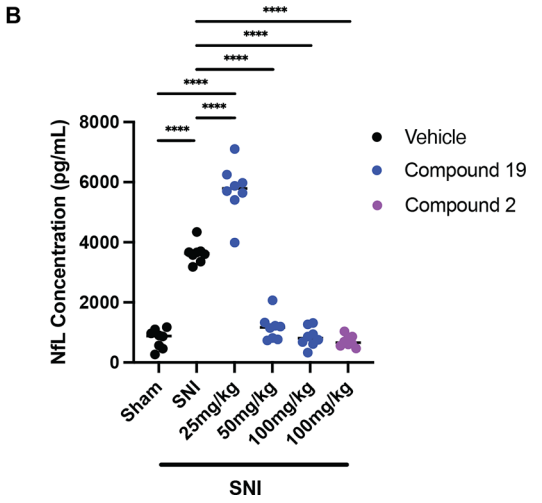

Figure 6. *In vivo* demonstration of compound **19** dose-dependent efficacy and subinhibitory effect in a mouse SNI model. (A) Schematic of BID dosing of **2** and **19** before and after a SNI. (B) Median plasma NfL concentration (pg/mL) following BID dosing of various doses of **2** (purple) or **19** (blue) compared to vehicle (black). (C) Plasma concentration taken at the terminal end point of the study. The table reports total plasma concentration (ng/mL) mean ± SD and a target engagement (TE) ratio, which is defined as TE ratio = (plasma concentration)/(protein binding corrected mouse DRG EC_{50}). Each group had $n = 8$ animals and individual animal data points are shown. A one-way ANOVA was performed ($p < 0.0001$) followed by a Tukey's multiple comparisons test (****, $p < 0.0001$).

improved metabolic stability and CYP and hERG inhibition relative to **19**.

Compound 19 Demonstrates Protection of Neurodegeneration *In Vivo* and *In Vitro* but Also Increases Markers of Neurodegeneration at Low Doses

With our SAR exploration highlighting the promising potency, low efflux, and modular DMPK properties for this series of azabenzimidazole-containing SARM1 inhibitors, we set our attention on characterizing the ability for such analogs to inhibit SARM1-mediated neurodegeneration in *in vivo* models. Based on the pharmacokinetics (PK) of **19** following a 100 mg/kg PO dose (Supplemental Figure 3), we projected that we could maintain sustained coverage of the mouse plasma protein binding adjusted DRG EC_{50} (445 ng/mL) with a BID dosing regimen (Figure 6A). Compound **19** was dosed orally in male C57BL/6 mice prior to and following spared sciatic nerve injury (SNI), a model of peripheral nerve degeneration/damage (Figure 6A). Following doses at 100 and 50 mg/kg BID, **19** demonstrated significant reduction in plasma neurofilament light chain (NfL), comparable both to the sham group and **2**, which was used as a positive control at 100 mg/kg BID based on literature precedent.[7] Surprisingly, a slight reduction in the **19** dose to 25 mg/kg BID demonstrated an increase in plasma NfL relative to the vehicle group (Figure 6B). Plasma concentrations of **19** were analyzed at the 30 h terminal time point (6 h post final dose) and demonstrated approximately 3-fold differences in mean plasma exposures between the individual three dosing groups of **19**. Using the *in vitro* EC_{50} from vincristine-induced neurodegeneration of mouse DRGs as a target engagement surrogate, only the 25 mg/kg group showed terminal plasma exposures below the *in vitro* efficacious concentration (Figure 6C). This same group demonstrated an increase in NfL levels above those of the vehicle group. Compound **2** demonstrated very high plasma concentrations and exposure multiples, which is consistent with reported PK data.[7]

Following our initial observation in Figure 6, several groups reported that SARM1 BEIs may paradoxically activate SARM1-mediated neurodegeneration under conditions of mild stress and suboptimal inhibitor concentration both *in vivo* and *in vitro*.[8,10,15−19] Given the observed increase in NfL following lower doses of **19**, we also tested the *in vitro* effects of **19** in a HEK293 cell line stably expressing full length SARM1 excluding the MTS.[26] When cells were treated with 60 μM CZ-48, a cell permeant NMN mimetic, very little cell death was observed relative to DMSO as assessed by CTG. However, addition of concentrations below 100 nM BEIs **19** and **2** caused significant cell death relative to DMSO alone. This cell-killing effect was completely reversed at higher concentrations of BEIs (Figure 7A). Under conditions of high stress, modeled here by treatment with 100 μM CZ-48, those same low concentrations of BEIs do not significantly exacerbate cell death (Figure 7B). A similar phenomenon was observed when primary rat DRGs were treated with CZ-48 and neurite health was assessed via high content imaging. In conditions of mild cell stress, modeled by a shorter incubation with CZ-48, lower concentrations of BEIs induced more cell death than CZ-48 alone. However, in conditions of higher cell stress, induced by a longer incubation with CZ-48, low concentrations of BEIs did not generate additional neurite damage (Figure 7C,D). Finally, we also recapitulated this phenomenon in human-derived induced pluripotent stem cell-derived cortical neurons (hiPSCs), which were treated with the SARM1 activator vacor.[27] Both **19** and **2** similarly demonstrated neurodegeneration, assessed via neurite length, at low concentrations while demonstrating neuroprotection at higher concentrations of BEIs. This effect was not observed when a higher concentration of vacor (10 μM) was used to induce cell death (Figure 7E,F). A similar effect was observed when hiPSC degeneration was instead assessed via CTG (data not shown).

Chemical Synthesis of 19

The synthesis of **19** is described in Scheme 1, and it allowed for modular SAR in several vectors around the scaffold. The indole moiety could be synthesized from commercially available **29**. Treatment with copper(I) cyanide followed by protection with SEMCl afforded **30** in 50% yield over two

https://doi.org/10.1021/acs.jmedchem.6c00352
J. Med. Chem. 2026, 69, 9521−9536

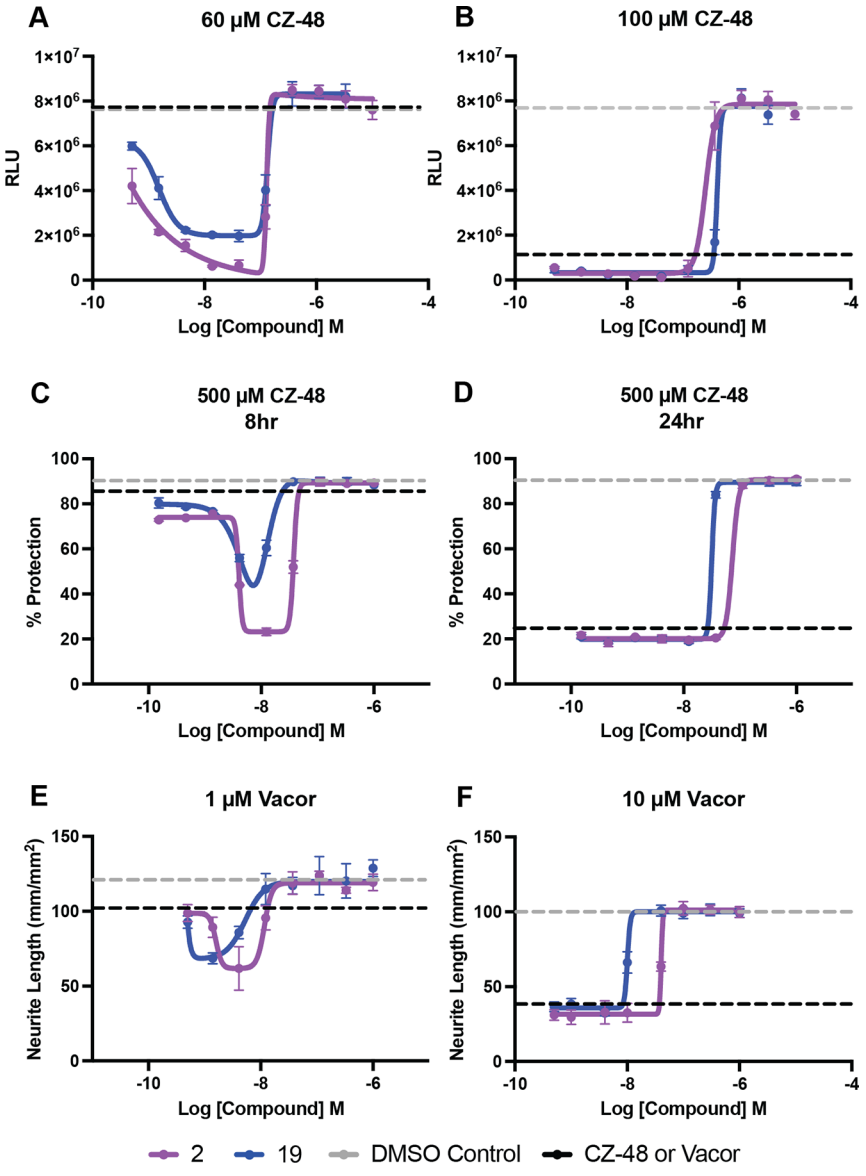

Figure 7. *In vitro* demonstration of subinhibitory effects with BEIs **2** and **19**. (A,B) HEK293 cell line expressing SARM1 was treated with either 60 or 100 μM CZ-48 and indicated concentrations of **19** or **2**. Cell protection was measured using CTG and compared to the cell death induced by CZ-48 alone (black) or DMSO (gray). (C,D) Primary rat DRG cells were exposed to both **19** and **2** and 500 μM CZ-48 for either 8 or 24 h, and the percentage of axons protected from degeneration was determined using high content imaging of beta III tubulin staining. (E,F) Neurite length of hiPSC-derived cortical neurons after exposure to either 1 or 10 μM Vacor and a dose response of **19** and **2**. The *y* axis has been normalized to *t* = 0, units mm/mm2. Data from A−F are representative from at least two independent experiments and are presented as mean ± SD.

steps. Finally, the pinacol boronate (**31**) could be selectively installed at C2 of the indole ring using Ir-mediated CH borylation with 60% isolated yield.

The remainder of the scaffold of **19** was synthesized starting with 2,4-dichloro-5-nitropyridine (**32**). Treatment with methylamine yielded 2-chloro-*N*-methyl-5-nitropyridin-4-amine in 77% yield, which was subsequently reduced to aniline **33** upon treatment with tetrahydroxydiboron and 4,4'-bipyridine.[28] The corresponding aniline was then cyclized under dehydrative conditions with methyl isonicotinate to afford azabenzimidazole **34** in 37% yield over 2 steps. Selective bromination ortho to the chlorine atom occurred upon treatment with LDA and 1,2-dibromotetrafluoroethane, to afford **35**, which served as a useful intermediate for modular functionalization. Buchwald−Hartwig amination with *N*,*N*-dimethylethylenediamine afforded **36**, which was then cross-coupled with suzuki partner **31** to afford **37** in 52% yield over 2 steps. Finally, SEM deprotection afforded **19** in a 76% yield.

DISCUSSION AND CONCLUSIONS

In conclusion, we have described the discovery and SAR of imidazo[4,5-*c*]pyridine-containing SARM1 inhibitors, initially identified via a novel FEP+ workflow. Modeling the ADPR-conjugated ligand binding derived from these BEIs is a particularly challenging case for physics-based modeling, with several reasons for the difficulty highlighted herein. This includes a high level of mobility observed in the ADPR moiety both in simulations and in experimental cocrystal structures, the absence of a reaction mechanism and rate component in such simulations, and the apparent flexibility within the binding site. Notably, W662 adopts a number of ligand-induced rotameric states both in literature examples and in the

https://doi.org/10.1021/acs.jmedchem.6c00352
J. Med. Chem. 2026, 69, 9521−9536

Scheme 1. Gram-scale Synthesis of 19[a]

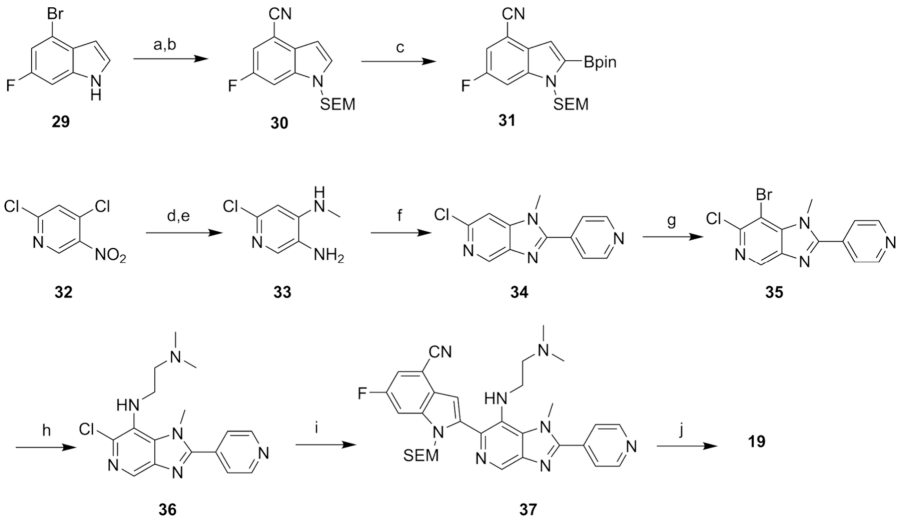

[a](a) CuCN, DMF, 140 °C, 72% yield; (b) SEMCl, DMF, Cs_2CO_3, 69% yield; (c) HBpin, Dtbpy, $[Ir(OMe)(cod)]_2$, THF, 65 °C, 60% yield; (d) methylamine, DIEA, THF, rt, 77% yield; (e) $B_2(OH)_4$, 4,4'-bipyridine, THF, rt; (f) methyl isonicotinate, PPA, 165 °C, 37% yield over 2 steps; (g) 1,2-dibromotetrafluoroethane, LDA, THF, −60 °C, 31% yield; (h) *N*,*N*-Dimethylethylenediamine, $Pd_2(dba)_3$, XantPhos, Toluene, 105-110 °C; (i) **31**, SPhos Pd G_3, Cs_2CO_3, Dioxane/water, 95-100 °C, 52% yield over 2 steps; (j) TFA, CH_2Cl_2, 76% yield

new examples reported here, which can further complicate molecular modeling. Nonetheless, development of this FEP+ workflow proved successful in identification of initial hit **7** and aided in the discovery of *in vivo* tool molecule **19** as well as **25**, which is further optimized for ADME properties and liabilities. We anticipate that this modeling workflow may have broader utility and could be adapted to other targets where enzyme-mediated precursor reactivity may be an effective strategy for pharmacological inhibition.[29]

Finally, the apparent SARM1 activation observed both *in vivo* and *in vitro* with low concentrations of **19**, which others have also reported with BEIs, may be a consequence of inhibiting SARM1 specifically in its active conformation. Inhibitor binding at the interfaces of neighboring TIR subunits in the double-stranded assembly traps the enzyme in a state poised for activity while blocking the active sites. In a hypothesis consistent with that originally postulated by Leahey et al., at substoichiometric inhibitor concentrations, the active TIR assembly is stabilized but not all NADase sites are blocked, leading to aberrant activation.[18] This suggests that high levels of sustained target coverage may be necessary for effective BEI-mediated neuroprotection and caution may be warranted when pursuing this mechanism in a clinical setting at suboptimal doses.

EXPERIMENTAL SECTION

General Procedures

All solvents and reagents were obtained from commercial sources and used without further purification unless indicated otherwise. Anhydrous solvents were purchased and used as supplied. Reactions were monitored by thin-layer chromatography (TLC) and visualized with a UV lamp (254 nm) and $KMnO_4$ stain. NMR spectra were obtained on a Bruker NEO 400 M spectrometer operating at 400 MHz. Chemical shifts are reported in parts per million (δ) from the tetramethylsilane resonance in the indicated solvent. LC-MS was taken with an Agilent 1260−6125B single quadrupole mass spectrometer using a Welch Biomate column (C18, 2.7 μm, 4.6 × 50 mm) or a Waters H-Class SQD2 system using a Welch Ultimate column (XB-C18, 1.8 μm, 2.1 × 50 mm) eluting with two kinds of mixed solvents [one is a mixture of solvents A (water with 0.05% FA) and B (ACN with 0.05% FA); another one is a mixture of solvents A (water with 10 mM NH_4HCO_3) and B (ACN)] using gradient elution. Detection was by DAD (254 and 210 and 280 nm). Ionization was by ESI. The spectra were analyzed using ChemStation software. Analytical HPLC was performed on the Waters ARC system either under acidic conditions on a YMC-Pack Pro column (C18 S3 μm, 12 nm, 150 × 2.0 mm) eluting with a mixture of solvents A (water with 0.05% FA) and B (ACN with 0.05% FA) or under basic conditions on an Agilent Poroshell HPH-C18 column (2.7 μm, 2.1 × 150 mm) eluting with a mixture of solvents C (water with 0.1% NH_4OH) and D (ACN with 0.1% NH_4OH) using a gradient elution. The detection was by DAD (254, 210, and 280 nm). Preparative HPLC was performed on the Gilson TRILUTION LC system using a Welch XB-C18 column (5 μm, 21.2 × 150 mm), eluting with two kinds of solvents [one is a mixture of solvents A (water with 0.1% FA) and B (ACN); another one is a mixture of solvents A (water with 10 mM NH_4HCO_3) and B (ACN)]. Flash chromatography was carried out on the Biotage Isolera Prime system using Welch WelFlash flash columns (40−63 μm) eluting with a mixture of solvents as indicated in the experimental procedures. Unless otherwise noted, the purity for compounds was judged to be >95% as determined by ^{1}H NMR and HPLC at 254 nm. All animal experiments were performed following the protocols evaluated and approved by the Institutional Animal Care and Use Committee (IACUC) of Pharmaron following the guidance of the Associate for Assessment and Accreditation of Laboratory Animal Care (AAALAC) (IVP-PD/PK-09132024; PK-M-07182023).

Synthesis of Compound 19

Step A: 6-Fluoro-1*H*-indole-4-carbonitrile. To a stirred solution of 4-bromo-6-fluoro-1*H*-indole (**29**, 10 g, 46.96 mmol) in DMF (50 mL) was added CuCN (6.31 g, 70.44 mmol) at 25 °C. The reaction mixture was stirred at 140 °C for 16 h under a nitrogen atmosphere. After cooling to rt, the reaction was quenched with water (50 mL) and extracted with EtOAc (80 mL × 2). The combined organic layers were dried over anhydrous Na_2SO_4, filtered, and evaporated. The residue was purified by silica gel column chromatography (THF:PE = 1:10 to 1:5) to afford 6-fluoro-1*H*-indole-4-carbonitrile (5.4 g, 72% yield). LCMS: m/z 161.1 $[M + H]^+$

Step B: 6-Fluoro-1-((2-(trimethylsilyl)ethoxy)methyl)-1*H*-indole-4-carbonitrile (30). To a stirred solution of 6-fluoro-1*H*-indole-4-carbonitrile (2.4 g, 14.99 mmol, 1.0 equiv) in DMF (24 mL,

https://doi.org/10.1021/acs.jmedchem.6c00352
J. Med. Chem. 2026, 69, 9521−9536

10 (v) and Cs_2CO_3 (7.33 g, 22.49 mmol, 1.5 equiv) was added SEMCl (3.75 g, 22.49 mmol, 1.5 equiv) at 0 °C. The reaction mixture was stirred at 25 °C for 4 h under a nitrogen atmosphere. The reaction was quenched with water (30 mL) and extracted with EtOAc (40 mL × 2). The combined organic layers were dried over anhydrous Na_2SO_4, filtered, and evaporated. The residue was purified by silica gel column chromatography (THF:PE= 0:1 to 1:10) to afford **30** (3.0 g, 69% yield). ^{1}H NMR (400 MHz, DMSO-*d6*) δ 8.18 (dd, J = 2.2, 1.4 Hz, 1H), 8.07 (d, J = 3.2 Hz, 1H), 7.89 (dd, J = 9.4, 2.2 Hz, 1H), 6.93 (dd, J = 3.2, 0.7 Hz, 1H), 5.88 (s, 2H), 3.71 (t, J = 8 Hz, 2H), 1.06 (t, J = 8 Hz, 2H), 0.16 (s, 9H)

Step C: 6-Fluoro-2-(4,4,5,5-tetramethyl-1,3,2-dioxaborolan-2-yl)-1-((2-(trimethylsilyl)ethoxy)methyl)-1*H*-indole-4-carbonitrile (31). To a stirred solution of **30** (3.0 g, 10.34 mmol, 1.0 equiv) in THF (60 mL) was added 4,4,5,5-tetramethyl-1,3,2-dioxaborolane (2.65 g, 20.68 mmol, 2.0 equiv) followed by the addition of 4,4'-di*tert*-butyl-2,2'-bipyridine (83 mg, 0.31 mmol, 0.03 equiv). Nitrogen was bubbled through the reaction mixture for 10 min. $[Ir(OMe)(cod)]_2$ (105 mg, 0.16 mmol, 0.015 equiv) was added, and the reaction mixture was stirred at 65 °C for 16 h under a nitrogen atmosphere. The solvent was evaporated, and the residue was purified by silica gel column chromatography (DCM:PE = 1:10 to 1:5) to afford **31** (2.67 g, 60% yield). ^{1}H NMR (400 MHz, DMSO-*d6*) δ 7.91 (dd, J = 9.9, 1.5 Hz, 1H), 7.70 (dd, J = 8.4, 2.2 Hz, 1H), 7.05 (d, J = 0.5 Hz, 1H), 5.80 (s, 2H), 3.42 (t, J = 7.8 Hz, 2H), 1.33 (s, 12H), 0.77 (t, J = 7.8 Hz, 2H), 0.13 (s, 9H).

Step D: 2-Chloro-*N*-methyl-5-nitropyridin-4-amine. Compound **32** (50 g, 0.26 mol) was added to a 1 L three-necked round-bottom flask and dissolved in THF (400 mL) under a N_2 atmosphere. Methylamine hydrochloride (20.99 g, 0.21 mol) was added to the mixture in one portion at 20−25 °C. DIEA (100.45 g, 0.78 mol) was then added to the mixture at 20−25 °C over 10 min, producing a yellow suspension that was stirred for 60 h. The mixture was filtered, and the filter cake was dried under vacuum at 45 °C. The crude product was slurried in *n*-heptane: EtOAc = 5:1 (5 V) for 12 h at 20 °C. Solids were filtered and the filter cake was washed with *n*-heptane:EtOAc = 5:1 (1 V). The solid was dried under vacuum to afford the title compound (37.5 g, 77% yield) as a yellow solid. LCMS (m/z): 185.9/187.9 $[M + H]^+$. ^{1}H NMR (400 MHz, $CDCl_3$) δ 9.01 (s, 1H), 8.35 (br s, 1H), 6.75 (s, 1H), and 3.06 (d, J = 5.2 Hz, 3H).

Step E: 6-Chloro-N4-methylpyridine-3,4-diamine (33). To a suspension of $B_2(OH)_4$ (40.62 g, 0.45 mol) in THF (136 mL) was added a solution of 4,4-bipyridine (0.707 g, 4.5 mmol) in THF (34 mL) dropwise, and the mixture was stirred at room temperature for 30 min. A solution of 2-chloro-*N*-methyl-5-nitropyridin-4-amine (17.0 g, 0.09 mol) in THF (170 mL) was added dropwise to the mixture, and the resulting mixture was stirred for 16 h. The mixture was then poured into ice water (500 mL) and combined with 2 additional reaction mixtures carried out under identical conditions in parallel. The pH of the mixture was adjusted to 8−9 with sat. $NaHCO_3$ (150 mL), forming a brown suspension. The mixture was then diluted with EtOAc (500 mL) and filtered through Celite, washing with an additional 200 mL of EtOAc. The organic layer was separated, and the aqueous layer was extracted again with EtOAc (1 L × 3). The combined organic layers were dried over sodium sulfate, filtered, and concentrated to afford **33** (39.0 g, 70.6 wt % purity by QNMR) as a brown solid, which was used directly to the next step without further purification. LCMS (m/z): 157.9/159.9 $[M + H]^+$.

Step F: 6-Chloro-1-methyl-2-(pyridin-4-yl)-1*H*-imidazo[4,5-*c*]pyridine (34). To a 500 mL three-necked round-bottomed flask was added PPA (195 mL) followed by **33** (39.0 g, crude) in one portion at room temperature. The resulting mixture was heated to 85−90 °C, and methyl isonicotinate (33.94 g, 0.247 mol) was added in one portion. The resulting mixture was heated to 165−170 °C for 3 h. The mixture was then cooled to 85−90 °C over about 1 h, and ice-cold water (500 mL) was added. The mixture was cooled to 20 °C and extracted with EtOAc (500 mL × 3). The combined organic layers were dried over sodium sulfate, filtered, and concentrated. The crude product was slurried with *n*-heptane:EtOAc (5:1, 5 V) for 12 h. The solids were then collected via filtration and dried to afford **34** (25 g, 37% yield over 2 steps) as an orange solid. LCMS (m/z): 244.9/246.9 $[M + H]^+$. ^{1}H NMR (400 MHz, DMSO-*d6*) δ 8.83 (m, 3H), 7.98 (s, 1H), 7.91 (dd, J = 4.4, 1.6 Hz, 1 H), 3.95 (s, 3H)

Step G: 7-Bromo-6-chloro-1-methyl-2-(pyridin-4-yl)-1*H*-imidazo[4,5-*c*]pyridine (35). To a solution of **34** (10.0 g, 40 mmol) in THF (950 mL) at −65 °C was added LDA (32.7 mL, 2M) dropwise over 20 min. The resulting brownish-red suspension was stirred at this temperature for 1 h. To the mixture was then added a solution of 1,2-dibromotetrafluoroethane (12.74 g, 50 mmol) in THF (50 mL) dropwise over 15 min. The solution was then stirred at −65 °C for a further 2 h and then warmed to −10 to 0 °C over 30 min. To the mixture was added water (200 mL), and the mixture was stirred for 30 min. This mixture was then combined with that of an identical reaction carried out in parallel, and the THF was removed *in vacuo*. The mixture was then extracted with DCM (300 mL × 3), and the combined organic layers were dried over sodium sulfate, filtered, and concentrated. The product was purified via silica gel chromatography (0−5% MeOH in DCM) to afford **35** (13.0 g, 31% yield) as a gray solid. LCMS (m/z): 322.8/324.8 $[M + H]^+$. ^{1}H NMR (400 MHz, DMSO-d_6) δ 8.84 (m, 3H), 7.83 (d, J = 6 Hz, 2H), 4.10 (s, 3H).

Step H: *N*1-(6-chloro-1-methyl-2-(pyridin-4-yl)-1*H*-imidazo-[4,5-*c*]pyridin-7-yl)-*N*2,*N*2-dimethylethane-1,2-diamine (36). To a 250 mL round-bottom flask containing toluene (120 mL) under argon were added **35** (3.0 g, 9 mmol), *N*,*N*-dimethylethylenediamine (4.09 g, 50 mmol), XantPhos (2.15 g, 3.7 mmol), and Cs_2CO_3 (9.06 g, 28 mmol). To this mixture was added $Pd_2(dba)_3$ (1.7 g, 1.9 mmol), and the mixture was stirred at 105−110 °C for 16 h. The mixture was cooled to room temperature and combined with 2 additional reaction mixtures performed in parallel under identical conditions. The combined mixture was filtered, and the filtrate was concentrated. The residue was purified by silica gel chromatography (0−5% MeOH in DCM) to afford **36** (10.0 g, 84% purity) as a brownish-red solid, which was used in the following step without further purification. LCMS (m/z): 330.9/332.9 $[M + H]^+$.

Step I: 2-(7-((2-(Dimethylamino)ethyl)amino)-1-methyl-2-(pyridin-4-yl)-1*H*-imidazo[4,5-*c*]pyridin-6-yl)-6-fluoro-1-((2-(trimethylsilyl)ethoxy)methyl)-1*H*-indole-4-carbonitrile (37). Five reactions were carried out in parallel. To a 250 mL round-bottom flask containing dioxane (80 mL) and water (16 mL) were added **36** (2.0 g, 6 mmol assumed), **31** (3.02 g, 7 mmol), and Cs_2CO_3 (5.91 g, 0.018 mol). To the mixture was then added SPhos Pd G_3 (1.42 g, 1.8 mmol) in one portion. The mixture was stirred under nitrogen at 95−100 °C for 1 h. The mixture was cooled to room temperature, and the 5 parallel reaction mixtures were combined. The mixture was filtered and concentrated. The residue was then purified by silica gel chromatography (0−20% MeOH in DCM) to afford **37** (8.5 g, 52% yield over 2 steps) as a red solid. LCMS (m/z): 585.2 $[M + H]^+$.

Step J: 2-(7-((2-(Dimethylamino)ethyl)amino)-1-methyl-2-(pyridin-4-yl)-1*H*-imidazo[4,5-*c*]pyridin-6-yl)-6-fluoro-1H-indole-4-carbonitrile (19). To a 250 mL round-bottom flask were added **37** (8.5 g, 15 mmol) and DCM (85 mL). To the mixture was added TFA (42.5 mL) in one portion at 20−25 °C, and the mixture was stirred for 1 h. The mixture was concentrated, and to the residue was added NH_3 (7 M in MeOH) (85 mL). The resulting suspension was stirred for 1 h, additional NH_3 (7 M in MeOH) (85 mL) was added followed by water (50 mL), and the mixture stirred for 10 min. The layers were separated, and the aqueous layer was further extracted with DCM (100 mL × 3). The combined organic layers were dried over sodium sulfate, filtered, and concentrated. The resulting crude product was purified by preparative HPLC (C18, reverse phase, H_2O/MeCN with NH_4OH + NH_4HCO_3 modifiers) to afford **19** (5.2 g, 76% yield) as a yellow solid. HPLC Purity: 99.6% (210 nm), 100% (254 nm); LCMS (ESI): m/z 455.2 $[M + H]^+$; ^{1}H NMR (400 MHz, DMSO-d_6) δ 12.34 (s, 1H), 8.90 − 8.79 (m, 3H), 7.92 (dd, J = 4.6, 1.6 Hz, 2H), 7.57 (m, 2H), 7.44 (s, 1H), 4.73 (t, J = 6.6 Hz, 1H), 4.23 (s, 3H), 3.27 (m, 2H), 2.58 (m, 2H), 2.26 (s, 6H). ^{19}F NMR (376 MHz, DMSO-d_6) δ −120.1 (1F). ^{13}C NMR (100 MHz, $CDCl_3$) δ: 159.7, 157.3, 154.4, 150.6, 141.5, 139.1, 138.1, 136.9, 135.5, 130.3, 128.3, 123.5, 117.8, 113.3, 113.0, 103.0, 102.7, 102.4, 99.5, 58.9, 48.5,

https://doi.org/10.1021/acs.jmedchem.6c00352
J. Med. Chem. 2026, 69, 9521−9536

45.5, 33.6. HRMS (ESI: M+H): calc. for $C_{25}H_{23}FN_8$ 455.2105, found 455.2118.

NAD-Glo Biochemical Assay

All reagents were prepared in assay buffer containing 25 mM HEPES at pH 7.4, 10 mM KCl, 10 mM $MgCl_2$, and 0.1% BSA. 200 nL of compound or DMSO was added to the 384-well plate (Perkinelmer, 6007290) in duplicate using Echo dispensing. Then, 10 μL of 160 nM SARM1 protein was added to the 384-well plate and incubated for 5 min at 25 °C. Then, 5 μL of 200 nM NMN (Sigma-Aldrich, N3501) working solution was added to the 384-well plate. After a 20 min incubation, 5 μL of 120 nM NAD (Sigma-Aldrich, N1636) working solution was added to the 384-well plate and the plate was incubated for 45 min at 25 °C. The final concentrations of SARM1, NMN, and NAD are 80 nM, 50 μM, and 30 μM, respectively.

After 45 min, 20 μL of 0.8% formic acid was added to quench the reaction. The quenched reaction was then diluted 40× using assay buffer, mixed, and transferred to a new 384-well plate. Then, 10 μL of NAD/NAD-Glo detection reagent (Promega, G9027) was added to each well, mixed, and incubated at room temperature for 30 min. Luminescence was measured on the Envision (PerkinElmer), and data was analyzed using GraphPad Prism to fit curves using Sigmoidal, 4PL, and X is log (concentration)

SARM1 TIR Domain SPR

Binding of small molecules to the immobilized SARM1 TIR domain was assayed on a Biacore 8K+ (Cytiva) using a Series S Streptavidin (SA) chip (Cytiva) at 25 °C (Compartment and Sensor Surface). Prior to each run, the 8K+ system was equilibrated using two "Change Solutions" of 1× HBS-P+ (Teknova) buffer. The SA chip surface was conditioned over three cycles consisting of three successive 60 s pulses of 1 M NaCl and 50 mM NaOH at a flow rate of 30 μL/min. Following conditioning, the 8K+ system was equilibrated into SPR running buffer (25 mM HEPES pH 7.4, 10 mM KCl, 10 mM $MgCl_2$, 1 mM TCEP, 500 μM NAD 0.05% Tween 20, 2% DMSO). 10 μg/mL biotinylated SARM1 TIR domain running buffer was injected onto sample flow cells at 5 μL/min for 500 s to produce an immobilization level of 4000−5000 response units (RU) followed by injections of 10 μg/mL biocytin in running buffer over all flow cells for 120 s at a flow rate of 30 μL/min. Prior to kinetic analysis, the immobilized SARM1 TIR protein was allowed to stabilize for 4000 s at a flow rate of 100 μL/min followed by 10 startup cycles consisting of a 90 s injection of SPR running buffer at 100 μL/min followed by 120 s of dissociation. For each small molecule, an eight point dose response of small molecule (1 or 10 μM top concentration, 2-fold dilutions) was injected using "single cycle kinetics" injections for 90 s at a flow rate of 100 μL/min and was allowed to dissociate for 7000 s. Before and after dose responses of small molecules, the activity of immobilized SARM1 was assessed by injection of a single saturating concentration of a positive control compound. Due to the rapidly decreasing activity of immobilized protein and slow dissociation of small molecules, only a single small molecule dose response was run on each channel of the chip surface.

Sensorgrams were processed with Cytiva Biacore Insight Evaluation Software (v6.0.7.1750) with Extended Screening expansion. Solvent correction was performed using a four-point calibration from 1.5 to 2.8% DMSO. Data were double referenced, injection and pump spikes were manually removed from sensorgrams, and the data were fit globally by nonlinear regression to a simple 1:1 Langmuir binding model without bulk refractive index (RI) to determine association/dissociation rate constants (k_a, k_d), analyte binding capacity (R_{max}), and the equilibrium K_d. Where dissociation rate constants were faster than 10^{-2} s^{-1}, the equilibrium dissociation constant and R_{max} values were determined by steady state affinity fitting. R_{max} values obtained during kinetic or steady state analysis represented 90 to 110% of the theoretical R_{max}, value indicating a surface activity of 90−100%, which agrees well with the surface activity control (90−100% activity). Sensorgrams and 1:1 binding model curve fits were exported from Insight Evaluation Software and replotted in GraphPad Prism.

Inducible SAM-TIR HEK293 Assay

A stable cell line containing the human SARM1 gene with only the SAM and TIR domains was generated into a Jump-In T-REx HEK293 cell background. These Jump In T-REx HEK293 cells/SAM-TIR (SAM-TIR HEK293 cells) were cultured in high glucose-DMEM media (Gibco, 11965092) containing 10% certified FBS (VivaCell BIOSCIENCES, C2720−0500), 0.5 mg/mL G418 (Thermofisher, 10131035), 5 μg/mL Blasticidin (Thermofisher, A1113902), and 1% penicillin-streptomycin at 37 °C, 5% CO_2 in a cell culture incubator.

SAM-TIR HEK293 cells were seeded into a 384-well plate at a density of 3,500 cells/well and incubated for 21 h at 37 °C with 5% CO_2. Compounds or a DMSO control were then added, n = 2 wells per concentration, and incubated for 1 h. Following that, doxycycline (Sigma, D3072) was added to a final concentration of 1 μg/mL to the cell culture plate for 24 h. After a 30 min equilibration to room temperature, Cell Titer-Glo (CTG) working solution was prepared according to instructions (Promega, G7572) and allowed to equilibrate to 25 °C. Then, 20 μL of CTG reagent was added into each well and incubated at RT for 15 min with shaking. The plates were read on an Envision (PerkinElmer) plate reader, and data were analyzed using GraphPad Prism to fit curves using Sigmoidal, 4PL, X is log (concentration).

Full Length SARM1 HEK293 CTG Assay

A stable cell line containing the human SARM1 gene without the MTS domain, corresponding to amino acids 28−724, was cloned into a HEK293 cell background. These "hSARM1 HEK293" cells were cultured in high glucose DMEM (Gibco, 11965092) containing 10% FBS (Gibco, 10091−148), 0.5 mg/mL G418 (Thermofisher, 10131031), and 1% penicillin-streptomycin at 37 °C and 5% CO_2 in a cell culture incubator.

On the first day of the assay, hSARM1 HEK293 cells were seeded into a 384-well plate (Greiner, 781080) at a density of 1,500 cells/35 μL/well. The following day, cells were incubated with 40 nL of compound for 1 h before 5 μL/well CZ-48 (MCE, HY-129522) was added to the appropriate final concentration and incubated overnight at 37 °C. The next day, plates were removed from the incubator and allowed to equilibrate to RT for around 10 min. Cell Titer-Glo (CTG) working solution was prepared according to instructions and allowed to equilibrate to 25 °C. Then, 20 μL of CTG reagent was added into each well and centrifuged with 1,000 rpm for 30 s and incubated at RT for 15 min with shaking. The plates were read on an Envision (PerkinElmer) plate reader, and data were analyzed using GraphPad Prism. Data were fit using nonlinear fit; bell-shaped X is log(concentration) functions.

Mouse and Rat DRG

Cell Isolation and Culturing. Pregnant female Sprague−Dawley rats at 15.5 days postcoitus were asphyxiated by CO_2 prior to cervical dislocation. The dorsal root ganglia (DRG) were isolated from embryos and kept on ice in Leibovitz's 15 medium (Solarb, LA9510). Rat DRGs (rDRGs) were dissociated by incubation in TrypLE Express (Gibco, 12604) at 37 °C for about 30 min and then Leibovitz's 15 medium with 10% FBS was added. Mouse DRGs (mDRGs) were prepared in a similar fashion except that they were collected from pregnant female C57BL6 mice at 13.5 days postcoitus and mDRGs were dissociated with Papain dissociation system kits for 10 min according to the protocol (Worthington, LK003150). mDRGs were then transferred into a Petri dish that was precoated with poly-D-lysine (Gibco, A3890401) and incubated 37 °C for 2 min.

Following digestion and filtration with a 100 μm cell strainer, DRGs were centrifuged and resuspended in complete medium containing neurobasal medium (Gibco, 21103049), 2% B-27 serum-free supplement (Gibco, 17504−044), 2 mM L-glutamine (Gibco, 25030−081), 2 μM 5-fluoro-2'-deoxyuridine (Sigma, F0503), 2 μM uridine (Sigma, U3003), 50 ng/mL 2.5S NGF (R&D, 556-NG-100), and 100 U/mL penicillin-streptomycin (Gibco, 15140). Cells were then counted and diluted in complete medium to a final concentration of 1×10^7 cells/mL. A 0.5 μL drop of cell suspension was then added into each well of a 96-well plate that had been

https://doi.org/10.1021/acs.jmedchem.6c00352
J. Med. Chem. 2026, 69, 9521−9536

precoated with poly-L-lysine (Sigma, P4832) overnight and laminin (5 ug/mL) (Thermofisher, 23017015) for 2 h. Following a 10−15 min incubation at 37 °C, 100 μL of complete medium was added to each well of the 96-well plate, which was then maintained in vitro at 37 °C and 5% CO_2 for 7 days for rat and 10 days for mice.

Vincristine Method. Compounds were made into 10 mM stock solutions and then diluted 3-fold with 100% (v/v) DMSO. Intermediate solutions were then prepared in a complete medium. Vincristine solution (MCE, HY-N0488) was prepared into 40 μM DMSO stock solution and then diluted 50 fold in complete medium. Compounds and vincristine solution, each 5.55 μL, were added to each well of the plate, with a final concentration of DMSO of 0.3%. High control and low control were prepared by dilution of 100% DMSO and 40 μM vincristine, respectively, and 11.1 μL of controls were added to the appropriate wells of the cell plate. The plate was then incubated for 48 h at 37 °C before being processed for immunohistochemistry.

CZ-48 Method. Compounds were prepared as described above. A 200 mM stock solution of CZ-48 (MCE, HY-129522) was prepared in DMSO and then diluted to 10× in a complete medium. The medium was replaced with a complete medium containing the compounds. After 1 h treatment at 37 °C with the compounds, 5.55 μL of CZ-48 was added to a final concentration of 500 μM. High control and low control was prepared by dilution of 100% DMSO and 10 mM CZ-48, respectively. The cells were then incubated for 8 or 24 h at 37 °C before being processed for immunohistochemistry.

Immunohistochemistry. After treatment with either vincristine or CZ-48 and compounds, the medium was aspirated, and the plate was washed two times with DPBS. Cells were fixed with 40 μL of 4% PFA for 10 min at RT followed by ice cold DPBS washes. Cells were then permeabilized with 40 μL 0.5% Triton X-100 for 10 min followed by washes with DPBS. Samples were then blocked for 30 min in DPBS with 5% FBS (Gibco, 10099141), 2% BSA (Sigma, A1933), and 0.1% Tween-20 (Sigma, P1379) followed by an overnight incubation with both Anti-Beta III Tubulin (Abcam, ab41489) and Anti-NeuN (Abcam, ab104225) primary antibodies at 4 °C. Primary antibodies were then removed and cells were washed with DPBS. Cells were then incubated with Goat Anti-Chicken (Abcam, ab150169) and Goat Anti-Rabbit (Abcam, ab150080) secondary antibody for 2 h RT. The solution was then aspirated and washed with DPBS. Each well of the 96-well plate was sealed with 50 μL of 90% glycerol. Images of 96-well plate were acquired using a High Content Analysis System (Operetta CLS, PerkinElmer).

Data Processing. The % protection of each well was calculated following the formula $P = (1 - (S_{Deg}/S_{total})) \times 100\%$ where S_{Deg} is the degenerated fiber surface area per well and S_{total} is the total fiber surface area per well. Data were analyzed by using GraphPad Prism. Standard assays were fit using Sigmoidal, 4PL, X is log(concentration), and subinhibitory experiments were fit using a nonlinear fit; bell-shaped X is log(concentration) functions.

hiPSC-Derived Cortical Neurons

384-well PDL-coated plates (PerkinElmer, 6057500) were coated with laminin (1 μg/mL; Sigma, L2020) in DPBS (Gibco, 14190−144) for 1 h at 37 °C and 5% CO_2. Human iPSC-derived cortical neurons, generated from iPSCs harboring an NGN2 expression cassette, were plated at 3 days *in vitro* at 3000 cells/well in 30 μL cortical maturation (CM) medium containing ROCKi (10 μM; Abcam, ab144494). The CM medium consists of Neurobasal Plus Medium (Gibco, 12348−017), B27-Plus (1X; Gibco, A3582801), BDNF (10 ng/mL; Peprotech, 450−02), NT-3 (10 ng/mL; Peprotech, 450−03), laminin (1 μg/mL; Sigma, L2020), and doxycycline (2 μg/mL; Sigma, D9891). The cells were incubated overnight at 37 °C in 5% CO_2. One day later, 30 μL/well CM was added, and the cells were maintained for 7 more days in culture.

Neurons were then treated with a range of compound concentrations, 8-point 3-fold dilution, for 1 h at 37 °C, 5% CO_2, before the addition of vacor (1 or 10 μM; Chem Service Inc., N13738) (n = 4 wells per condition). Live cell images were acquired at 10× in phase contrast over 48 h using an Incucyte SX5 (Sartorius) housed in an incubator (37 °C, 5% CO_2) and analyzed using the Incucyte Neurotrack Analysis software module. Neurite length at T = 48 h calculated as a percent of its starting point at T = 0 and normalized to vehicle control (DMSO) was graphed using GraphPad Prism and used to calculate EC50 values. Standard assays were fit using Sigmoidal, 4PL, where X is log(concentration) and subinhibitory experiments were fit using a nonlinear fit; bell-shaped X is log(concentration) functions.

Spared Sciatic Nerve Injury (SNI) model

Six-to-eight week old male C57BL/6 mice (n = 8 per group, vendor: Beijing Vital River Co. LTD) were used in a spared sciatic nerve injury model (SNI) to assess axonal protection during treatment with SARM1 inhibitors *in vivo*. Briefly, SNI was induced in isoflurane anesthetized animals by severing the tibial and peroneal nerves while the sural nerve was left intact. Animals were dosed orally twice daily (BID) at the indicated doses and a dose was administered 2 h before the SNI surgery. The vehicle for compound **19** was 0.5% MC (4000 cP) and 0.25% Tween 80 in water, and for compound **2**, it was 2.5% DMSO, 10% Cremophore EL, pH 7 sterile water containing 5% dextrose. Plasma was obtained at 28 h post-SNI surgery and plasma neurofilament light chain (NfL) was measured by ELISA according to the manufacturer's protocol (Quanterix CAT#:10−7002).

■ ASSOCIATED CONTENT

Supporting Information

The Supporting Information is available free of charge at https://pubs.acs.org/doi/10.1021/acs.jmedchem.6c00352.

Supplemental figures, synthetic schemes, protein expression, purification, crystallographic data, DMPK and computational protocols; and spectral data: NMR and LC-MS/HPLC traces for compounds **6**−**28** (PDF)

Molecular formula strings (CSV)

■ AUTHOR INFORMATION

Corresponding Author

Adam M. Levinson − *Schrödinger, Inc., New York, New York 10036, United States*; orcid.org/0000-0002-2202-5255; Email: adam.levinson@schrodinger.com

Authors

Steven K. Albanese − *Schrödinger, Inc., New York, New York 10036, United States*

Brittany E. Hopkins − *Schrödinger, Inc., New York, New York 10036, United States*

Andrea M. Olland − *Schrödinger, Inc., Framingham, Massachusetts 01702, United States*

Alexis Fairman − *Bristol Myers Squibb, East Cambridge, Massachusetts 02141, United States*

Nadim Shaikh − *Schrödinger, Inc., Hyderabad, Telangana 500032, India*

Shulu Feng − *Schrödinger, Inc., New York, New York 10036, United States*

Mahesh Thakkar − *Schrödinger, Inc., Hyderabad, Telangana 500032, India*

Andreas Verras − *Schrödinger, Inc., New York, New York 10036, United States*

Alexey Dementiev − *Schrödinger, Inc., Framingham, Massachusetts 01702, United States*

Ward G. Walkup, 4th − *Schrödinger, Inc., Framingham, Massachusetts 01702, United States*; orcid.org/0000-0002-0385-6256

Christian Atsriku − *Schrödinger, Inc., New York, New York 10036, United States*

https://doi.org/10.1021/acs.jmedchem.6c00352
J. Med. Chem. 2026, 69, 9521−9536

Harathi D. Srinivas − *Schrödinger, Inc., Hyderabad, Telangana 500032, India*
Wayne Allen − *Schrödinger, Inc., Framingham, Massachusetts 01702, United States*
Khuram Ashraf − *Schrödinger, Inc., Framingham, Massachusetts 01702, United States*
Pieter H. Bos − *Schrödinger, Inc., New York, New York 10036, United States;* orcid.org/0000-0002-8710-4771
Peng Hsiao − *Schrödinger, Inc., San Diego, California 92122, United States*
Kyle Kroeck − *Schrödinger, Inc., Framingham, Massachusetts 01702, United States*
Zhijian Liu − *Schrödinger, Inc., New York, New York 10036, United States*
Anu Nagarajan − *Schrödinger, Inc., New York, New York 10036, United States*
Christopher T. Szlenk − *Schrödinger, Inc., New York, New York 10036, United States*
Mats Svensson − *Schrödinger, Inc., New York, New York 10036, United States*
Zachary Lee Johnson − *Schrödinger, Inc., New York, New York 10036, United States*
Kanishk Kapilashrami − *Schrödinger, Inc., New York, New York 10036, United States*
Stephen Rubino − *Schrödinger, Inc., Cambridge, Massachusetts 02142, United States*
Andrew Kaplan − *Bristol Myers Squibb, East Cambridge, Massachusetts 02141, United States*

Complete contact information is available at: https://pubs.acs.org/10.1021/acs.jmedchem.6c00352

Author Contributions

‡S.K.A., B.E.H., and A.M.O. share equal contribution.

Notes

The authors declare the following competing financial interest(s): All authors are current or former employees of Schrodinger, Inc. or Bristol Myers Squibb and may own shares of stock and/or stock options in these companies.

■ ACKNOWLEDGMENTS

The authors thank Aleksey Gerasyuto, Jonathan Macdonald, Kristian Jensen, Zhe Nie, Tyler Day, Veerabahu Shanmugasundaram, Scott Watterson, Allie Muthukumar, Paul Scola, and Robert Abel for review and feedback on this manuscript and for helpful conversations. The authors would like to thank Ellie Tomasson, Jacob Kim, and Abby Mariga for providing iPSC cortical neuron progenitors. We thank James Evans for creative support in figure design. The authors thank Mark Labow for critical discussions and insights. We thank Hua Zhou, Nan Dong, Xinya Duan, Liyan Fang, and Mingrui Li from Viva Biotech for experimental support. We thank Chao Rong and Xiaoming Xu from Pharmaron for help with spectral data collection. We thank Lei Wen, Yajun Ma, and Min Lu from Pharmaron for experimental support. We thank Julian Nommé, Céline Ronin, and Fabrice Ciesielski from Novalix for protein production and crystallography support.

■ ABBREVIATIONS

ACN, Acetonitrile; **ADME**, Absorption, Distribution, Metabolism, Excretion; **ADPR**, Adenosine Diphosphate Ribose; **ARM**, Armadillo Repeat; **BCRP**, Breast Cancer Resistance Protein; **BEI**, Base Exchange Inhibitor; **CIPN**, Chemotherapy-Induced Peripheral Neuropathy; **cod**, 1,5-Cyclooctadiene; **CTG**, CellTiter-Glo; **CYP**, Cytochrome P450; **dba**, Dibenzylideneacetone; **DIEA**, Diisopropylethylamine; **DMF**, Dimethylformamide; **DRG**, Dorsal Root Ganglion; **Dtbpy**, 4,4′-Di-*tert*-butyl-2,2′-dipyridyl; **FA**, Formic Acid; **FEP**, Free-Energy Perturbation; **hERG**, Human Ether-à-go-go-Related Gene; **hiPSC**, Human Induced Pluripotent Stem Cell; **HPLC**, High-Performance Liquid Chromatography; **IV**, Intravenous; **LD**, Lithium Diisopropylamide; **LLE**, Lipophilic Ligand Efficiency; **LM**, Liver Microsome; **MCS**, Maximum Common Substructure; **MDR1**, Multidrug Resistance Protein 1; **MTS**, Mitochondrial Targeting Sequence; **MUE**, Mean Unsigned Error; **NAD^+**, Nicotinamide Adenine Dinucleotide; **NfL**, Neurofilament Light; **NMN**, Nicotinamide Mononucleotide; **PDB**, Protein Data Bank; **PPA**, Propylphosphonic anhydride; **SAM**, Sterile Alpha Motif; **SAR**, Structure−Activity Relationship; **SARM1**, Sterile Alpha and Toll/Interleukin-1 Receptor Motif 1; **SEM**, (Trimethylsilyl)ethoxymethyl; **SNI**, Sciatic Nerve Injury; **SPhos**, 2-Dicyclohexylphosphino-2′,6′-dimethoxybiphenyl; **SPR**, Surface Plasmon Resonance; **TE**, Target Engagement; **TFA**, Trifluoroacetic Acid; **THF**, Tetrahydrofuran; **TIR**, Toll/Interleukin-1 Receptor; **TLC**, Thin layer chromatography; **XantPhos**, 4,5-Bis(diphenylphosphino)-9,9-dimethylxanthene

■ REFERENCES

(1) Coleman, M. P.; Höke, A. Programmed Axon Degeneration: From Mouse to Mechanism to Medicine. *Nat. Rev. Neurosci.* **2020**, *21* (4), 183−196.
(2) Conforti, L.; Gilley, J.; Coleman, M. P. Wallerian Degeneration: An Emerging Axon Death Pathway Linking Injury and Disease. *Nat. Rev. Neurosci.* **2014**, *15* (6), 394−409.
(3) Krauss, R.; Bosanac, T.; Devraj, R.; Engber, T.; Hughes, R. O. Axons Matter: The Promise of Treating Neurodegenerative Disorders by Targeting SARM1-Mediated Axonal Degeneration. *Trends Pharmacol. Sci.* **2020**, *41* (4), 281−293.
(4) Sambashivan, S.; Freeman, M. R. SARM1 Signaling Mechanisms in the Injured Nervous System. *Curr. Opin. Neurobiol.* **2021**, *69*, 247−255.
(5) Bratkowski, M.; Xie, T.; Thayer, D. A.; Lad, S.; Mathur, P.; Yang, Y.-S.; Danko, G.; Burdett, T. C.; Danao, J.; Cantor, A.; Kozak, J. A.; Brown, S. P.; Bai, X.; Sambashivan, S. Structural and Mechanistic Regulation of the pro-Degenerative NAD Hydrolase SARM1. *Cell Rep.* **2020**, *32* (5), No. 107999.
(6) Hughes, R. O.; Bosanac, T.; Mao, X.; Engber, T. M.; DiAntonio, A.; Milbrandt, J.; Devraj, R.; Krauss, R. Small Molecule SARM1 Inhibitors Recapitulate the SARM1−/− Phenotype and Allow Recovery of a Metastable Pool of Axons Fated to Degenerate. *Cell Rep.* **2021**, *34* (1), No. 108588.
(7) Bratkowski, M.; Burdett, T. C.; Danao, J.; Wang, X.; Mathur, P.; Gu, W.; Beckstead, J. A.; Talreja, S.; Yang, Y. S.; Danko, G.; Park, J. H.; Walton, M.; Brown, S. P.; Tegley, C. M.; Joseph, P. R. B.; Reynolds, C. H.; Sambashivan, S. Uncompetitive, Adduct-Forming SARM1 Inhibitors Are Neuroprotective in Preclinical Models of Nerve Injury and Disease. *Neuron* **2022**, *110* (22), 3711−3726.
(8) Green, S. A.; Smith, R. T.; Grandner, J. M.; Zeng, M.; Del Bel, M.; Zhu, B.-Y.; Liang, J.; Braun, M.-G.; Sudhamsu, J.; Wallweber, H. A.; Boenig, G.; Murray, J.; Shen, X.; Zhang, R.; Lai, K. W.; Delwig, A.; Breboneria, M. A.; Ly, J.; Ganti, A.; Nespi, M.; Weber, M.; Leahey, R.; Hinz, F. I.; Chan, B. K. Optimization of Brain Penetrant SARM1 Orthosteric Inhibitors and Discovery of Their Paradoxical Sub-inhibitory Activation. *ACS Med. Chem. Lett.* **2025**, *16* (6), 1147−1154.
(9) Shi, Y.; Kerry, P. S.; Nanson, J. D.; Bosanac, T.; Sasaki, Y.; Krauss, R.; Saikot, F. K.; Adams, S. E.; Mosaiab, T.; Masic, V.; Mao,

X.; Rose, F.; Vasquez, E.; Furrer, M.; Cunnea, K.; Brearley, A.; Gu, W.; Luo, Z.; Brillault, L.; Landsberg, M. J.; DiAntonio, A.; Kobe, B.; Milbrandt, J.; Hughes, R. O.; Ve, T. Structural Basis of SARM1 Activation, Substrate Recognition, and Inhibition by Small Molecules. *Mol. Cell* **2022**, *82* (9), 1643−1659.
(10) Giroud, M.; Kuhn, B.; Steiner, S.; Westwood, P.; Mendel, M.; Mani, A.; Pinard, E.; Haap, W.; Grether, U.; Caramenti, P.; Rombach, D.; Zambaldo, C.; Ritter, M.; Schmid, P.; Gasser, C.; Aregger, N.; Séchet, N.; Topp, A.; Bilyard, M.; Malnight-Alvarez, A.; Plitzko, I.; Hilbert, M.; Kalayil, S.; Burger, D.; Bonardi, C.; Saal, W.; Haider, A.; Wittwer, M. B.; Brigo, A.; Benz, J.; Keaney, J. Discovery of a Potent SARM1 Base-Exchange Inhibitor with in Vivo Efficacy. *J. Med. Chem.* **2025**, *68* (6), 6558−6575.
(11) Bosanac, T.; Hughes, R. O.; Engber, T.; Devraj, R.; Brearley, A.; Danker, K.; Young, K.; Kopatz, J.; Hermann, M.; Berthemy, A.; Boyce, S.; Bentley, J.; Krauss, R. Pharmacological SARM1 Inhibition Protects Axon Structure and Function in Paclitaxel-Induced Peripheral Neuropathy. *Brain* **2021**, *144* (10), 3226−3238.
(12) Geisler, S.; Doan, R. A.; Strickland, A.; Huang, X.; Milbrandt, J.; DiAntonio, A. Prevention of Vincristine-Induced Peripheral Neuropathy by Genetic Deletion of SARM1 in Mice. *Brain* **2016**, *139* (Pt 12), 3092−3108.
(13) Geisler, S.; Huang, S. X.; Strickland, A.; Doan, R. A.; Summers, D. W.; Mao, X.; Park, J.; DiAntonio, A.; Milbrandt, J. Gene Therapy Targeting SARM1 Blocks Pathological Axon Degeneration in Mice. *J. Exp. Med.* **2019**, *216* (2), 294−303.
(14) Gould, S. A.; Gilley, J.; Ling, K.; Jafar-Nejad, P.; Rigo, F.; Coleman, M. Sarm1 Haploinsufficiency or Low Expression Levels after Antisense Oligonucleotides Delay Programmed Axon Degeneration. *Cell Rep.* **2021**, *37* (11), No. 110108.
(15) Mani, A.; Mendel, M.; Westwood, P.; Bonardi, C.; Saal, W.; Topp, A.; Bilyard, M.; Brigo, A.; Wittwer, M. B.; Benz, J.; Kuhn, B.; Haider, A.; Giroud, M.; Keaney, J. SARM1 Base-Exchange Inhibitors Induce SARM1 Activation and Neurodegeneration at Low Doses. *NPJ. Drug Discovery* **2025**, *2* (1), 12.
(16) Zhang, W.; Zhou, Q.; Zhang, J.; Wang, J.; Wu, Q.; Zheng, S.; Wang, X. SARM1 Activation Promotes Axonal Degeneration via a Two-Step Phase Transition. *Nat. Chem. Biol.* **2025**, 435.
(17) Reardon, H. T.; Guijas, C.; Clapper, J. R.; Callender, J. A.; Kozina, E. M.; Sarabia, F. J.; Hutton, C.; Herbst, D. M.; Andalis, T.; Perehinets, L.; Henry, C. L.; Lebold, T. P.; Kummer, D. A.; Blankman, J. L.; Wiener, J. J. M.; Simonsen, K. B.; Samad, T. A. Base Exchange Inhibitors of SARM1 Form Mononucleotide Adducts and Activate SARM1 in Vivo. *bioRxiv* **2025**.
(18) Leahey, R. R.; Weber, M.; Cho, C. H.; Hur, S. K.; Cramer, A.; Manzanares, K.; Babin, B.; Boenig, G.; Kring, T.; Liu, L.; Cui, Y.; Ganti, A.; Evans, J. P.; Nespi, M.; Ly, J.; Nugent, A. A.; Green, S. A.; Chan, B. K.; Hoogenraad, C. C.; Delwig, A.; Hinz, F. I. Therapeutic Safety Implications of SARM1 Active Site Inhibitors: Subinhibitory Concentrations Cause Neurodegeneration. *NPJ. Drug Discovery* **2025**, *2* (1), 21.
(19) Lundbäck, T.; Chandrasekar, V.; Gu, C.; Ju, H.; McAdam, R.; Palomero, M.; Sader, K.; Peter, B.; Wissler, L.; Nevin, P.; Foster, E.; Jamier, T.; Manjappa, P.; Johansson, C.; Sandmark, J.; Ding, M.; Persson-Kry, A.; Mitra, S.; Satir, T. M.; Bilican, B.; Messa, M.; Fraser, G.; Linley, J.; Plant, H.; Moore, R.; Seifert, T.; Lerche, M.; Raynochek, C.; Nilsson, E.; Majbour, N.; Lucey, R.; de Oliveira, T. M.; Wang, Q.; Chessell, I.; Breccia, P.; Jarvis, R. The Rise and Fall of SARM1 Base-Exchange Inhibitors. *bioRxiv* **2025**.
(20) Wang, L.; Wu, Y.; Deng, Y.; Kim, B.; Pierce, L.; Krilov, G.; Lupyan, D.; Robinson, S.; Dahlgren, M. K.; Greenwood, J.; Romero, D. L.; Masse, C.; Knight, J. L.; Steinbrecher, T.; Beuming, T.; Damm, W.; Harder, E.; Sherman, W.; Brewer, M.; Wester, R.; Murcko, M.; Frye, L.; Farid, R.; Lin, T.; Mobley, D. L.; Jorgensen, W. L.; Berne, B. J.; Friesner, R. A.; Abel, R. Accurate and Reliable Prediction of Relative Ligand Binding Potency in Prospective Drug Discovery by Way of a Modern Free-Energy Calculation Protocol and Force Field. *J. Am. Chem. Soc.* **2015**, *137* (7), 2695−2703.
(21) Ross, G. A.; Lu, C.; Scarabelli, G.; Albanese, S. K.; Houang, E.; Abel, R.; Harder, E. D.; Wang, L. The Maximal and Current Accuracy of Rigorous Protein-Ligand Binding Free Energy Calculations. *Commun. Chem.* **2023**, *6* (1), 222.
(22) Konze, K. D.; Bos, P. H.; Dahlgren, M. K.; Leswing, K.; Tubert-Brohman, I.; Bortolato, A.; Robbason, B.; Abel, R.; Bhat, S. Reaction-Based Enumeration, Active Learning, and Free Energy Calculations to Rapidly Explore Synthetically Tractable Chemical Space and Optimize Potency of Cyclin-Dependent Kinase 2 Inhibitors. *J. Chem. Inf. Model.* **2019**, *59* (9), 3782−3793.
(23) *Schrödinger Release 2023−4: Maestro*; Schrödinger, LLC, New York, NY, 2023.
(24) Lu, C.; Wu, C.; Ghoreishi, D.; Chen, W.; Wang, L.; Damm, W.; Ross, G. A.; Dahlgren, M. K.; Russell, E.; Von Bargen, C. D.; Abel, R.; Friesner, R. A.; Harder, E. D. OPLS4: Improving Force Field Accuracy on Challenging Regimes of Chemical Space. *J. Chem. Theory Comput.* **2021**, *17* (7), 4291−4300.
(25) Beck, T. C.; Beck, K. R.; Morningstar, J.; Benjamin, M. M.; Norris, R. A. Descriptors of Cytochrome Inhibitors and Useful Machine Learning Based Methods for the Design of Safer Drugs. *Pharmaceuticals (Basel)* **2021**, *14* (5), 472.
(26) Zhao, Z. Y.; Xie, X. J.; Li, W. H.; Liu, J.; Chen, Z.; Zhang, B.; Li, T.; Li, S. L.; Lu, J. G.; Zhang, L.; Zhang, L.-H.; Xu, Z.; Lee, H. C.; Zhao, Y. J. A Cell-Permeant Mimetic of NMN Activates SARM1 to Produce Cyclic ADP-Ribose and Induce Non-Apoptotic Cell Death. *iScience* **2019**, *15*, 452−466.
(27) Loreto, A.; Angeletti, C.; Gu, W.; Osborne, A.; Nieuwenhuis, B.; Gilley, J.; Merlini, E.; Arthur-Farraj, P.; Amici, A.; Luo, Z.; Hartley-Tassell, L.; Ve, T.; Desrochers, L. M.; Wang, Q.; Kobe, B.; Orsomando, G.; Coleman, M. P. Neurotoxin-Mediated Potent Activation of the Axon Degeneration Regulator SARM1. *Elife* **2021**, *10*, No. e72823.
(28) Hosoya, H.; Misal Castro, L. C.; Sultan, I.; Nakajima, Y.; Ohmura, T.; Sato, K.; Tsurugi, H.; Suginome, M.; Mashima, K. 4,4'-Bipyridyl-Catalyzed Reduction of Nitroarenes by Bis(neopentylglycolato)diboron. *Org. Lett.* **2019**, *21* (24), 9812−9817.
(29) Stott, A. J.; Bürli, R. W.; Doyle, K. J.; Dickson, L.; Hewer, R. C.; Pickford, P.; Roberts, M. J.; Waters-Hall, R.; Wu, Y.; Zebisch, M.; Rangel, V.; Geitmann, M.; Matthews, K.; Brice, N. L.; Carlton, M.; Dawson, L. A.; Harvey, J. R. M. Discovery of Potent, Selective, and Brain-Penetrant Small Molecule CD38 Inhibitors. *ACS Med. Chem. Lett.* **2026**, *17* (2), 259−265.

https://doi.org/10.1021/acs.jmedchem.6c00352
J. Med. Chem. 2026, 69, 9521−9536